



Dark spots and cold jets in the polar regions of Mars: New clues from a thermal model of surface CO₂ ice

C. Pilorget^{a,*}, F. Forget^a, E. Millour^a, M. Vincendon^b, J.B. Madeleine^a

^a Laboratoire de Météorologie Dynamique, CNRS/UPMC/IPSL, 4 place Jussieu, BP99, 75252 Paris Cedex 05, France

^b Department of Geological Sciences, Brown University, Providence, RI 02912, USA

ARTICLE INFO

Article history:

Received 5 June 2010

Revised 18 January 2011

Accepted 18 January 2011

Available online 21 March 2011

Keywords:

Mars, atmosphere

Mars, climate

Mars, polar caps

ABSTRACT

Observations of the martian CO₂ ice cap in late winter and spring have revealed exotic phenomena. Unusual dark spots, fans and blotches form as the south-polar seasonal CO₂ ice cap retreats. The formation mechanisms of these features are not clearly understood. Theoretical models suggest that photons could penetrate deep into the CO₂ ice down to the regolith, leading to basal sublimation and gas and dust ejection. We have developed a detailed thermal model able to simulate the temporal evolution of the regolith-CO₂ ice layer-atmosphere column. It takes into account heat conduction, radiative transfer within the ice and the atmosphere, and latent heat exchange when there is a phase transition. We found that a specific algorithm, fully coupling these three components, was needed to properly predict ice sublimation below the surface. Our model allows us to determine under what conditions basal sublimation is possible and thus when and where it can occur on Mars. Our results show that basal sublimation is possible if we consider large pathlengths and very little dust content within the ice. Moreover, the model can explain how dark spots can appear very early after the end of the polar night at high latitudes. We also evaluate the importance of the different parameters in our simulations. Contrary to what was suggested by theoretical models, the role of seasonal thermal waves is found to be limited. Solar radiation alone can initiate basal sublimation, which therefore only depends on the CO₂ ice properties. Three main modes were identified: one where condensation/sublimation only occurs at the surface (in the case of small grains and/or high dust content), one where basal sublimation is possible (large pathlengths and very little dust content) and an intermediate mode where sublimation within the ice may occur. We suggest that these different modes could be keys to understanding many processes that occur at the surface of Mars, like the anticryptic area behavior or the recent reported activity in gullies.

© 2011 Elsevier Inc. All rights reserved.

1. Introduction

On Mars, about one third of the atmosphere (composed of 95% CO₂) condenses during fall and winter to form polar caps. Because of pressure and temperature conditions at the surface, there is no CO₂ liquid phase and solid CO₂ directly condenses and sublimates. During spring, the insolation increases and the seasonal polar cap disappears gradually (except in the southern very high latitudes where a small perennial polar cap remains). The Thermal Emission Spectrometer (TES) onboard the Mars Global Surveyor (MGS) spacecraft has characterized the recession date as defined by the “crocus date” and the thermal and visual properties of the seasonal

polar caps (Kieffer et al., 2000; Kieffer and Titus, 2001). The Observatoire pour la Mineralogie, l'Eau, les Glaces, et l'Activite (OMEGA) onboard Mars Express has acquired repeated spectral data of the polar ices and dust in the visible and near infrared and mapped their distribution (Bibring et al., 2004; Langevin et al., 2006, 2007). The MGS Mars Orbiter Camera (MOC) and Mars Reconnaissance Orbiter (MRO) High Resolution Imaging Science Experiment (HiRISE) have returned high-resolution images of the polar regions revealing numerous exotic features. During seasonal polar cap recession, dark spots and fans appear on the surface. Many of the features look like exposures of subfrost soil, and have been interpreted as such (Malin and Edgett, 2000; Supulver et al., 2001), but the Thermal Emission Imaging System (THEMIS) observations showed that they remain near the temperatures expected for solid CO₂ for days to months, and therefore must be in intimate contact with, or composed of, solid CO₂ (Kieffer et al., 2006). A proposed explanation is that solar radiation penetrates into the CO₂ slab, heats the regolith and sublimates the base of the CO₂ slab, which then levitates above the ground by gas pressure. Gas tries to

* Corresponding author. Present address: Institut d'Astrophysique Spatiale, Université de Paris Sud 11, 91405 Orsay, France.

E-mail addresses: Cedric.Pilorget@lmd.jussieu.fr (C. Pilorget), Francois.Forget@lmd.jussieu.fr (F. Forget), Ehouarn.Millour@lmd.jussieu.fr (E. Millour), Mathieu_Vincendon@brown.edu (M. Vincendon), Jean-Baptiste.Madeleine@lmd.jussieu.fr (J.B. Madeleine).

escape, and when a path to the surface is created, CO₂ gas and dust are ejected and form these dark spots (Kieffer, 2007; Piqueux et al., 2003; Portyankina et al., 2010). This process results from the characteristics and behavior of solid CO₂ on Mars, which are unlike those for any natural ice on Earth. In this paper, we present a model that helps us to investigate these features and some of their possible formation mechanisms. Our main objectives are:

- (1) To study the different sublimation processes that can occur during spring.
- (2) To test the “cold jets” theory and see under which conditions the CO₂ slab can sublimate at its base.
- (3) To try to understand why dark spots appear in some locations and not everywhere at the same time.
- (4) To study the earliest seasonal dark spots and see how much time they need to form, and under which conditions. A case study was made of the Manhattan Island area at 85°S.
- (5) To test and improve the scenarios of this “dark spots cycle” with our results.

2. Model description

2.1. General description

To simulate the detailed seasonal evolution of a layer of CO₂ ice at a given location on Mars, we have developed a 1D model able to compute the temporal evolution of a column composed of an underlying regolith, a CO₂ ice layer, and the atmosphere above. It is an extension of a 1D version of the general circulation model from Laboratoire de Meteorologie Dynamique (Forget et al., 1999). The model is fully described in the following sections.

In practice, the atmospheric model allows one to simulate a radiative convective equilibrium atmospheric profile and is used to compute the incident radiation on the surface and the sensible heat exchange between the surface and the atmosphere (see below). Below the surface, we have developed a model that solves heat exchange, radiative transfer and mass evolution equations in the CO₂ slab as well as in the regolith. We used a finite volume approach to solve the equations, with a timestep of 0.001 martian day (89 s). The model takes into account the solar flux (0.1–5 μm), the incident thermal flux, the thermal emission, the sensible heat flux, the geothermal heat flux, and the latent heat flux when there is a phase transition (Fig. 1).

2.2. Vertical grid

The vertical computational grid used in our model is a dynamic layer grid where individual layers have distinct thermal and optical properties. Their total number is fixed; therefore, the number of regolith layers is equal to the difference between the total number of layers and the number of CO₂ ice layers which evolves with time as CO₂ condenses and sublimates. When a layer sublimates totally, this layer disappears and another layer of regolith is added at the bottom of the domain at the temperature of the above layer. In the case of condensation, if the first layer is full of CO₂ ice, another layer of CO₂ ice is added above it, and the last layer of regolith is removed. Tests were performed to check the energy balance and showed that it has no effect on the results. The layer thickness is set to 1 cm. Simulations with thinner layers showed no significant change in the results. Since measured thermal inertias on Mars range from 30 to 2000 J s^{-1/2} m⁻² K⁻¹, the grid used had to be such that it captures diurnal and annual thermal waves in such media. For the regolith part, the skin depth corresponding to oscillation period P would be for an homogeneous (infinite) soil (volumetric specific heat C and conductivity λ):

$$\delta_p = \frac{I}{C} \left(\frac{P}{\pi} \right)^{1/2} \quad (1)$$

If we want to take into account the seasonal thermal waves, we thus have to consider a minimum depth of 0.13 m for $I = 30$ and 8.69 m for $I = 2000$ ($C = 10^6$ J K⁻¹ m⁻³). In our simulations, we thus use a 10 m thick surface composed of a thousand 1 cm layers.

2.3. Incident solar visible radiation

2.3.1. Atmospheric dust scattering

Visible and near infrared radiative effects of dust are taken into account by computing the radiative transfer in two different bands: 0.1–0.5 and 0.5–5 μm with a Toon et al. (1989) radiative transfer code. The Delta-Eddington approximation is applied in order to better simulate the forward scattering peak of dust particles. We use the Ockert-Bell et al. (1997) dust properties in our model. However, other dust properties could be used if needed (e.g. Wolff et al., 2009).

Atmospheric dust scattering plays a major role when the Sun is low on the horizon, as is common in polar regions. In the case of the Manhattan Island area (85°S), the solar zenith angle is never less than about 60°. More interestingly, Fig. 2 shows that the solar zenith angle is never less than about 85° when the first dark spots appear around Ls 175° (Kieffer et al., 2006; Aharonson, 2004).

Simulations with a Monte-Carlo code using a spherical geometry (Vincendon and Langevin, 2010) show that at that time, for an atmospheric dust optical depth set to 0.1 (Vincendon et al., 2008) and dust confined to the first 6 km of the cold polar atmosphere, at least one half of the solar flux that reaches the surface is scattered by atmospheric dust. The incidence angles of these photons can be very different from the incidence angle of the direct solar beam. This is important since in the slab model, for instance, the Fresnel reflection coefficient quickly rises from 0.5 to 1 for solar angles higher than 85° (Fig. 3). Simulations performed with the Monte-Carlo code give us the distribution of these incidence angles for various solar angles. To simplify, we computed an effective incidence angle for these photons by calculating an effective albedo due to specular reflection and then derived the corresponding angle

$$R_{\text{eff}} = \frac{\int_0^{\pi/2} f(i)R(i)di}{\int_0^{\pi/2} f(i)di} \quad (2)$$

with R_{eff} the effective albedo, $f(i)$ the fraction of photons reaching the surface with an incidence angle i and $R(i)$ the Fresnel reflection coefficient for an incidence angle i . In our model, we calculate the penetration of photons from the direct flux with an incidence angle equal to the solar angle, and the penetration of photons from the scattered flux with this computed effective incidence angle. The incident solar flux can be nonzero when the Sun is below the skyline. For an atmospheric dust optical depth set to 0.1 and dust confined to the first 6 km of the atmosphere, solar flux cannot be neglected at incidence angles up to 95° (at 91°, about 1% of the incoming solar flux reaches the surface and at 95° it is less than 0.1%).

We tuned our model to fit with these simulation results when the solar zenith angle is greater than 90° (see Fig. 4). The cosine of the solar zenith angle is also corrected to take into account the spherical geometry and the refraction by the atmosphere (Forget et al., 1999):

$$\mu_0 = \frac{\sqrt{1224\mu_0^2 + 1}}{35} \quad (3)$$

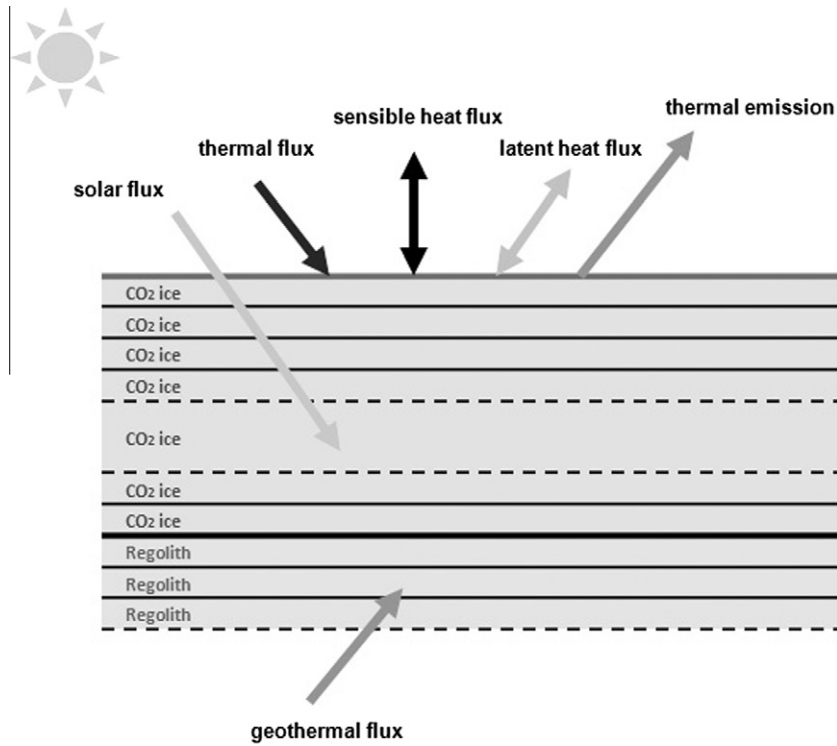


Fig. 1. Energy terms used in our model (solar flux (0.1–5 μm), incident thermal flux, thermal emission, sensible heat flux, geothermal heat flux, and latent heat flux when there is a phase transition).

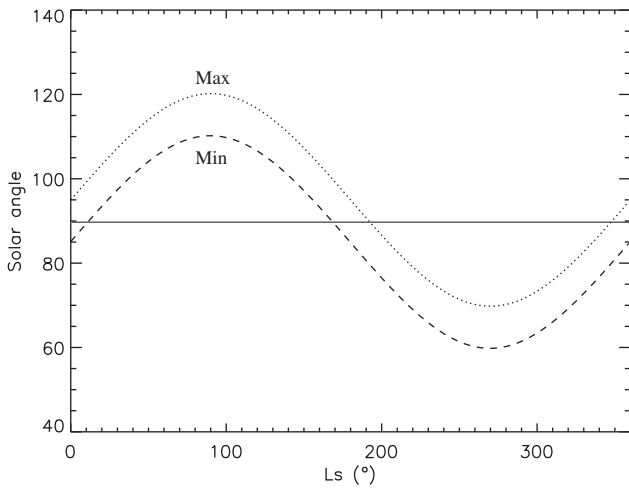


Fig. 2. Evolution of the solar zenith angle at 85°S latitude. Dotted line represents the maximum angle and the dashed line the minimum angle. At this latitude, the end of the polar night occurs around Ls 168°. The Sun remains close to the horizon during spring.

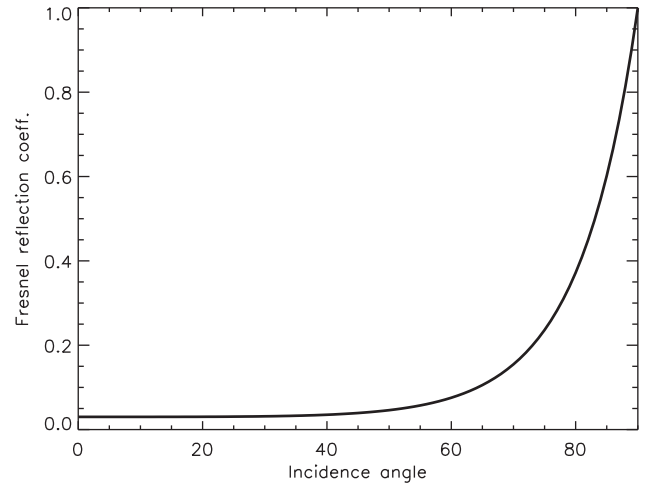


Fig. 3. Evolution of the Fresnel reflection coefficient of a flat CO₂ ice layer with solar incidence angle, as defined by Eqs. (11)–(13). The reflection coefficient increases very quickly after 60°, a typical case for the polar regions. Fresnel reflection can therefore severely limit solar radiation penetration in these areas.

2.3.2. Effect of slope

We use the model developed by Spiga and Forget (2008); Spiga and Forget (2008) to compute the influence of the slope and its orientation on our results. This allows us to compute the direct incoming flux D , the scattered flux by the atmosphere S and the reflected flux from the neighboring terrains R .

$$F_0 = D + S + R \tag{4}$$

We introduce here σ_s which is the sky-view factor that quantifies the proportion of the sky in the half-hemisphere “seen” by the slope that is not obstructed by the surrounding terrains (assumed to be flat).

$$\sigma_s = \frac{1 + \cos(\theta)}{2} \tag{5}$$

where θ is the inclination of the slope. The thermal incident flux is computed assuming that the atmospheric thermal radiation is isotropic

$$F_{th} = \sigma_s F_{th0} + (1 - \sigma_s)E \tag{6}$$

with F_{th0} the incident thermal flux that would reach a flat terrain, E the thermal flux emitted by the surrounding terrains.

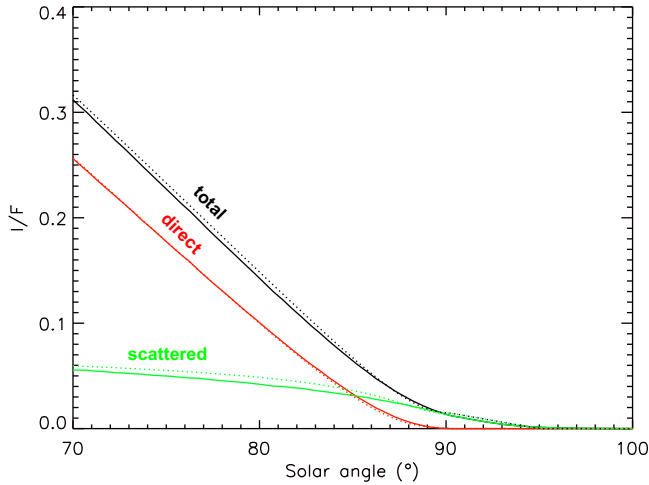


Fig. 4. Fraction of the solar flux (“ I/F ”) reaching the surface as a function of the solar zenith angle ($I/F=1$ for a Sun at zenith without atmosphere). The direct and scattered components of the solar flux reaching the surface are detailed (red and green curves respectively – total in black). For solar zenith angles greater than 85 more than half of the solar flux reaching the surface is due to aerosol scattering. After the terminator (no more direct component), aerosols still significantly illuminate the surface for a few degrees. Solid lines are results obtained through the use of the model and Mars dust parameters detailed in Vincendon and Langevin (2010), while the dashed lines represent the analytical model used in this study. (For interpretation of the references to color in this figure legend, the reader is referred to the web version of this article.)

2.4. Solar flux penetration

Two models have been used to test the different scenarios: a CO₂ “snow” model assuming that CO₂ is composed of scattering and absorbent grains and a CO₂ “slab ice” model assuming that CO₂ is an homogeneous absorbent medium. This latter model can be used to test different scenarios where the photon pathlengths are in the range of several tens of centimeters, as revealed in several areas by TES (Kieffer et al., 2000) and OMEGA (Langevin et al., 2007) observations. We ran the simulations with a CO₂ ice density of 1606 kg m⁻³ (which corresponds to a CO₂ ice without porosity).

2.4.1. CO₂ snow model

In this model, the grain size is specified, and then remains constant during the simulation rather than evolving with time. The mass fraction of dust grains in the CO₂ ice can be specified. However, to simplify the computation, dust scattering was treated as if dust particles were surrounded by vacuum. As for the atmosphere, we use the Ockert-Bell et al. (1997) optical parameters. Based on Langevin et al. (2007) we assume that H₂O ice grain content is negligible in the areas where the Kieffer (2007) scenario is likely to occur. CO₂ ice optical properties are taken from Quirico and Schmitt (1997) and Schmitt et al. (1998). Radiative transfer within the CO₂ ice is calculated with a Toon et al. (1989) radiative transfer code as in Williams et al. (2008). Our model uses Mie theory for single scattering by individual snow grains, together with the Delta-Eddington method for multiple scattering in a snowpack as in Warren et al. (1990), Hansen (1999) and Kieffer et al. (2000). To compute the optical depth of CO₂ and dust at a given wavelength, we assume

$$\tau_{\text{CO}_2} = \frac{3M_{\text{CO}_2} Q_{\text{ext}}^{\text{CO}_2}}{4\rho_{\text{CO}_2} r_{\text{eff}}^{\text{CO}_2}} \quad (7)$$

$$\tau_{\text{dust}} = \frac{3M_{\text{CO}_2} q_{\text{dust}} Q_{\text{ext}}^{\text{dust}}}{4\rho_{\text{dust}} r_{\text{eff}}^{\text{dust}}} \quad (8)$$

where M_{CO_2} is the mass of CO₂ ice, q_{dust} the mass fraction of dust, Q_{ext} the extinction coefficient, ρ the density, and r_{eff} the effective

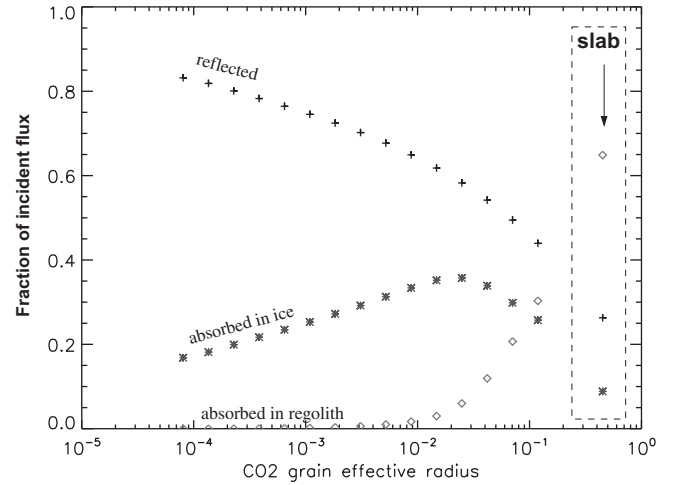


Fig. 5. Evolution of the interaction between the CO₂ ice layer and the solar flux as a function of CO₂ grain radius in meters (CO₂ snow model). Ice thickness = 0.6 m; incident solar angle = 60°; ground albedo = 0.24; no dust content. As the effective grain radius increases, the reflected part decreases and the part absorbed in the ice increases. However, photons are not yet able to reach the regolith until the effective radius is higher than about 1 mm. As the effective radius continues to increase, photons can go through the ice more easily and the part absorbed in the ice begins to decrease.

radius. In our simulations we assume $r_{\text{eff}}^{\text{dust}} = 1.5 \mu\text{m}$, $\rho_{\text{dust}} = 2000 \text{ kg m}^{-3}$ and $\rho_{\text{CO}_2} = 1606 \text{ kg m}^{-3}$. Finally the radiative transfer code returns the upward and downward fluxes at each level, which leads to

$$E_{\text{pen}}(z_2 - z_1) = F_{\text{up}}(z_2) - F_{\text{up}}(z_1) + F_{\text{down}}(z_1) - F_{\text{down}}(z_2) \quad (9)$$

with $E_{\text{pen}}(z_2 - z_1)$ the radiative energy deposited between z_1 and z_2 in W m^{-2} , $F_{\text{up}}(z)$ the upward flux at depth z , $F_{\text{down}}(z)$ the downward flux the depth z .

2.4.2. Translucent slab model

This model is an extreme case of the previous model, in which the CO₂ slab is an homogeneous absorbent medium. As photons reach the surface, some are reflected (Fresnel reflection) and the others penetrate into the ice. The latter are absorbed following a Beer–Lambert law. However, the way solar radiation penetrates and propagates in the ice depends not only on the properties of the medium, but also on the wavelength. To simplify the calculation we compute an effective CO₂ real optical index (Warren, 1986; Quirico and Schmitt, 1997; Schmitt et al., 1998; Hansen, 2005) and Beer–Lambert coefficient so that the reflection only depends on the incidence angle and the absorption of the solar radiation in the ice only depends on the distance covered by the photons. The penetration of solar energy was calculated as

$$\int_0^{\infty} S_{\lambda} (1 - R_{\lambda}) e^{-p/l_{\lambda}} d\lambda \quad (10)$$

where S_{λ} is the incident solar flux at the surface at a certain wavelength, R_{λ} the Fresnel reflection coefficient, p the pathlength from the surface along the refracted path and $l_{\lambda} = \lambda/4\pi n_i$ the absorption length. With these results, we computed an effective absorption coefficient k that does not depend on the wavelength and use it in our model. The solar radiation reaches the regolith whose albedo is fixed (mean value in the visible). The reflected fraction is partly absorbed on its way back and the rest escapes from the slab. In theory, as it reaches the surface, some of the flux is reflected into the slab. However, when the regolith albedo is low (less than 0.3 for instance) this effect is small. For this reason, we do not take into

account multiple reflections in the slab. Dust can also be added in the slab (see Fig. 6). We have for the Fresnel reflection

$$R = \frac{r_s^2 + r_p^2}{2} \quad (11)$$

where r_s is the Fresnel coefficient if the light is polarized with the electric field perpendicular to the incident plane and r_p the Fresnel coefficient if the light is polarized with the electric field parallel to the incident plane.

$$r_s = \frac{n_{\text{atm}} \cos(\theta_{\text{inc}}) - n_{\text{CO}_2} \cos(\theta_{\text{ref}})}{n_{\text{atm}} \cos(\theta_{\text{inc}}) + n_{\text{CO}_2} \cos(\theta_{\text{ref}})} \quad (12)$$

$$r_p = \frac{n_{\text{atm}} \cos(\theta_{\text{ref}}) - n_{\text{CO}_2} \cos(\theta_{\text{inc}})}{n_{\text{atm}} \cos(\theta_{\text{ref}}) + n_{\text{CO}_2} \cos(\theta_{\text{inc}})} \quad (13)$$

with $n_{\text{atm}} = 1$ and $n_{\text{CO}_2} = 1.4$ mean value in the visible (Warren, 1986; Quirico and Schmitt, 1997; Schmitt et al., 1998; Hansen, 2005). θ_{inc} and θ_{ref} are respectively the incident angle and the refracted angle, which are linked by the relation

$$n_{\text{atm}} \sin(\theta_{\text{inc}}) = n_{\text{CO}_2} \sin(\theta_{\text{ref}}) \quad (14)$$

For an incident flux, F_0

$$F_{\text{pen}}(1) = F_0(1 - R) \quad (15)$$

where R is the reflection coefficient for unpolarized light, $F_{\text{pen}}(1)$ the flux that penetrates into the first layer in W m^{-2} and F_0 the incident flux in W m^{-2} . For the following layers, with z_1 and z_2 , two different depths under the surface, and $z_1 < z_2$:

$$F_{\text{pen}}(z_2) = F_{\text{pen}}(z_1) e^{\left(\frac{-k(z_2 - z_1)}{\cos(\theta_{\text{ref}})}\right)} \quad (16)$$

with $F_{\text{pen}}(z)$ the flux that penetrates into a surface at a depth z in W m^{-2} , and k a constant depending on the properties of the material between z_1 and z_2 . Kieffer (2007) also computes the flux that reaches the regolith with respect to the depth and the incidence angle. Our results are consistent with theirs.

After solar radiation reaches the regolith, one fraction is reflected and the other penetrates into the regolith where it is absorbed in the first millimeters. We set the reflected angle to 45° , the average angle for a Lambertian reflection (see e.g. Vincendon et al., 2007, Fig. 1). The reflected fraction is then partly absorbed

into the ice before reaching the surface. We thus have at the interface between CO_2 ice and regolith

$$F_{\text{penref}}(z_{\text{interface}}) = F_{\text{pen}}(z_{\text{interface}}) A_{\text{grd}} \quad (17)$$

and

$$F_{\text{penref}}(z_1) = F_{\text{penref}}(z_2) e^{\left(\frac{-k(z_2 - z_1)}{\cos(\theta_{\text{ref}})}\right)} \quad (18)$$

with $z_{\text{interface}}$ the depth of the interface between CO_2 ice and the regolith in m, A_{grd} the regolith albedo, $F_{\text{penref}}(z)$ the reflected flux that penetrates into a surface at a depth z in W m^{-2} .

At the end we have:

$$E_{\text{pen}}(z_2 - z_1) = (F_{\text{pen}}(z_1) - F_{\text{pen}}(z_2)) + (F_{\text{penref}}(z_1) - F_{\text{penref}}(z_2)) \quad (19)$$

with $E_{\text{pen}}(z_2 - z_1)$ the radiative energy deposited between z_1 and z_2 in W m^{-2} .

2.4.3. Synthesis

Fig. 5 shows the reflected and absorbed fluxes in the two models. When we increase the grain size in the CO_2 snow model, the albedo decreases. More energy is absorbed by the ice plus regolith. When the size is over a few centimeters, the solar radiation can reach the regolith and the part of the flux that is absorbed in the ice decreases. The slab ice model appears to be a good way to simulate pathlengths in the range of several tens of centimeters.

For both models, we compute the energy that is absorbed in each layer and with that result, we calculate the temperature increase between z_1 and z_2

$$\frac{\partial T}{\partial t} = \frac{E_{\text{pen}}}{\rho C_p (z_2 - z_1)} \quad (20)$$

with E_{pen} the radiative energy deposited between z_1 and z_2 in W m^{-2} , C_p the heat capacity of the layer in $\text{J K}^{-1} \text{kg}^{-1}$, ρ the density, $z_2 - z_1$ the thickness of the layer in m.

However, the pressure is not constant within the slab, which is a critical point with regards to the phase transition (see Section 2.9).

2.5. Thermal infrared radiation absorption and emission

2.5.1. Downward atmospheric thermal flux

Gaseous CO_2 and airborne dust emit a thermal flux that reaches the surface. This thermal flux cannot penetrate more than a few millimeters into the CO_2 ice (Kieffer, 2007). In our model, it is treated as surface absorption.

2.5.2. Thermal emission

Thermal emission is equal to $\epsilon \sigma T_{\text{surf}}^4$ with σ the Stephan–Boltzmann constant ($\sigma = 5.67 \times 10^{-8} \text{W m}^{-2} \text{K}^{-4}$), T_{surf} the surface temperature and ϵ the spectrally averaged emissivity. We set $\epsilon = 0.9$ in the case of CO_2 ice covering the soil and $\epsilon = 0.95$ when there is no CO_2 ice (Forget et al., 1998). Surface temperature T_{surf} is determined assuming that CO_2 frost at the surface is in vapor pressure equilibrium with atmospheric CO_2 gas at surface pressure P_{surf} assuming a CO_2 mixing ratio of 95%.

2.6. Sensible heat flux

The sensible exchange of heat between the surface and the atmosphere is calculated as the product between the vertical gradient of temperature (estimated between the surface value and that in the first atmospheric layer), the surface drag coefficient (computed assuming a roughness length of 1 cm), and the wind velocity in the lowest level. This velocity is estimated using the

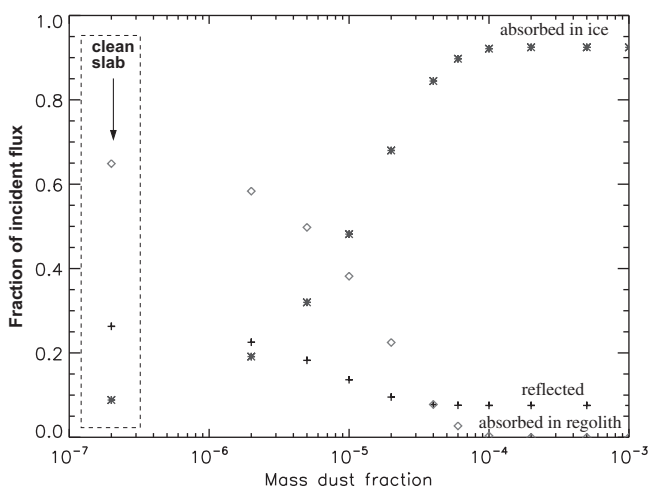


Fig. 6. Evolution of the interaction between the CO_2 ice layer and the solar flux as a function of dust content (slab model). Ice thickness = 0.6 m; incident solar angle = 60° ; ground albedo = 0.24. As the dust contamination increases, it becomes much more difficult for photons to penetrate into the ice. With a dust contamination of 10 ppm, less than 40% of solar radiation is absorbed by the regolith and with 100 ppm, it decreases to less than 1%.

boundary layer scheme described in Forget et al. (1999), assuming that the background wind velocity in the free atmosphere is 10 m s^{-1} . In practice the sensible heat flux is very small because of the low density of the martian atmosphere and the fact that the horizontal advection of heat is neglected.

2.7. Geothermal flux

Geothermal flux is set to a constant upward heat flux of 0.030 W m^{-2} , though estimates vary by a few mW m^{-2} (Schubert et al., 1992). The order of magnitude of this flux is generally negligible in the cumulative frost balance when compared with the other terms. Nevertheless, for facets in the shadow, it could accelerate the occurrence of the “crocus” day (i.e. the recession date) by typically one martian day.

2.8. Thermal conduction in ice and ground

For a solid, the time dependent diffusion equation leads to

$$\rho C_p \frac{\partial T}{\partial t} = -\nabla \vec{F}_c \quad (21)$$

where C_p is the specific heat (unit: $\text{J kg}^{-1} \text{K}^{-1}$), ρ the material's density in kg m^{-3} , \vec{F}_c is the conductive heat flux: $F_c = -\lambda \vec{\nabla} T$ (λ is the solid's heat conductivity, in $\text{W m}^{-1} \text{K}^{-1}$).

$$\rho C_p \frac{\partial T}{\partial t} = \nabla[\lambda \nabla T] \quad (22)$$

Thermal conduction is here considered as a one dimensional (1D) process. Temperature T of the soil is thus a function of time t and depth z , which must satisfy the following equation:

$$\rho C_p \frac{\partial T}{\partial t} = \frac{\partial}{\partial z} \left(\lambda \frac{\partial T}{\partial z} \right) \quad (23)$$

In the context of physical processes in the soil, the boundary conditions for this problem are

$$-\lambda \frac{\partial T}{\partial z}(z=0) + \Sigma F_{\text{other}} - \epsilon \sigma T^4 = 0 \quad (24)$$

at the surface and

$$-\lambda \frac{\partial T}{\partial z}(z=z_0) = F_{\text{geothermal}} \quad (25)$$

at the bottom of the domain.

Thermal conduction in the soil is computed as follows:

- Time integration is done via an implicit (first order) Euler scheme which approximates the differential equation $dT(t)/dt = F(T, t)$ as:

$$\frac{T^{(i+1)} - T^{(i)}}{\delta t} = F(T^{(i+1)}, t^{(i+1)}) \quad (26)$$

where superscripts denote time levels and δt the timestep.

- The lower boundary condition is included as such in the solver, but the upper boundary condition is not. Surface temperature is technically linked to atmospheric and ground processes which are coupled (via boundary condition in Eq. (24)). Rather than solving the coupled problem, it is uncoupled in a way that allows one to solve atmospheric and ground processes separately. The essential feature of the artificial uncoupling is that the atmospheric problem is first solved, yielding in the processes the value of surface temperature $T_{\text{surf}}^{(i+1)}$ at time $t^{(i+1)}$, which is then used as an input boundary condition for the soil heat diffusion problem.

2.9. CO₂ phase transition

2.9.1. Sublimation temperature

CO₂ condensation/sublimation temperature is taken from Hourdin et al. (1993). This relation tends to slightly underestimate the sublimation temperature in the pressure range compared to other relations (James et al., 1992). However a maximum difference of 2 K was noticed and simulation results are not significantly impacted.

$$T_{\text{sub}}(z) = \frac{1}{0.0734 - 0.000324 \log(0.01 P_{\text{CO}_2}(z))} \quad (27)$$

with P_{CO_2} the partial pressure of CO₂ in Pa. We take $P_{\text{CO}_2} = 0.95 P_{\text{surf}}$ at the surface. We assume that the pressure inside the slab at depth z is given by:

$$P_{\text{CO}_2}(z) = P_{\text{surf}} + \rho g z \quad (28)$$

with ρ the density of the ice in kg m^{-3} , g the gravity on Mars (3.72 m s^{-2}) and z the depth in m. Fig. 7 shows the evolution of the sublimation temperature with depth. In our case, CO₂ ice thickness can range from 10 cm at mid-latitudes to more than 70 cm in the polar regions. The difference between the sublimation temperature at the surface and the one at the bottom of the slab can be higher than 20 K in typical polar conditions.

2.9.2. CO₂ sublimation/condensation

Latent heat is released or absorbed as CO₂ condenses or sublimates such that:

$$L = -\frac{dm_{\text{CO}_2}}{dt} L_{\text{sub}}^{\text{CO}_2} \quad (29)$$

with $L_{\text{sub}}^{\text{CO}_2}$ the CO₂ latent heat of sublimation ($L_{\text{sub}}^{\text{CO}_2} = 5.9 \times 10^5 \text{ J kg}^{-1}$) and m_{CO_2} the mass of CO₂. For each layer, the difference between the temperature of the layer, after adding the increase due to solar energy absorption and computing conduction, and the sublimation temperature leads us to the amount of CO₂ ice that sublimates (if CO₂ ice is present) or condenses (if CO₂ gas is available):

$$dm_{\text{CO}_2}(i) = \frac{T_{\text{sub}}(i) - T_{\text{soil}}(i)}{L_{\text{sub}}^{\text{CO}_2}} \rho C_p \Delta z(i) \quad (30)$$

where $dm_{\text{CO}_2}(i)$ is the CO₂ mass variation in $\text{kg s}^{-1} \text{ m}^{-2}$, $T_{\text{soil}}(i)$ the predicted temperature (without taking into account the phase transition) in layer i in K, $T_{\text{sub}}(i)$ the sublimation temperature in K, Δt the timestep in s, C_p the CO₂ heat capacity in $\text{J K}^{-1} \text{ kg}^{-1}$, $\Delta z(i)$ the

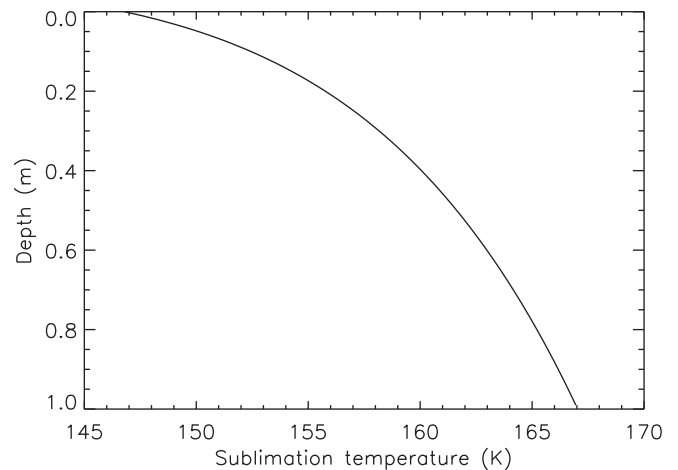


Fig. 7. Sublimation temperature in a CO₂ ice slab for surface pressure equal to 507 Pa. Material is an homogeneous CO₂ ice slab with a density of 1606 kg m^{-3} .

thickness of layer i in m. We actually compare the temperature of the layer, which is calculated at the middle of the layer, with the sublimation temperature, which is calculated at the base of the layer (or at the top of the layer for the first one, since sublimation occurs at the surface). Decreasing the thickness of the layers shows that this approximation had no significant effect on the results.

2.10. Algorithm

As we said previously, our model solves heat, radiation and mass evolution equations in the CO₂ ice and in the regolith. If we consider a translucent slab, solar radiation can easily penetrate. The regolith quickly heats and so does the CO₂ ice at the bottom of the slab. If the sublimation temperature is reached, we first need to convert the energy in excess to the amount of CO₂ that sublimates before computing the thermal conduction in the above layers. Thus we need to couple heat, radiation and mass evolution. The algorithm that we chose consists in computing the solar energy deposition in each layer, then doing a loop with the following processes:

1. Find the layer where the excess of energy is the highest compared to the sublimation point (or the lack of energy if we consider CO₂ layer where CO₂ gas is present, like the first layer for instance). It is the layer where sublimation (or condensation) is the most likely to occur.
2. Compute the latent heat related to this sublimation (or condensation).
3. Calculate the new thermal conduction coefficients and compute the new temperatures.
4. Return to step 1 as long as there is still an excess of energy (or a lack in the specified conditions).

These fluxes will be used later to calculate the sublimated or condensed amounts of CO₂ ice in each layer. Calculating processes this way guarantees that the thermal conduction is computed using realistic temperatures in the CO₂ ice that are never higher than the sublimation point.

2.11. Effect of gas in the layers

If basal sublimation occurs, a layer of gas forms between the CO₂ slab and the regolith, which modifies the thermal behavior of the slab. The conductivity of CO₂ gas is much lower than the conductivity of CO₂ ice ($\lambda_{\text{ice}}^{\text{CO}_2} = 0.65202 \text{ W m}^{-1} \text{ K}^{-1}$ at 144 K, $\lambda_{\text{gas}}^{\text{CO}_2} = 0.00590 \text{ W m}^{-1} \text{ K}^{-1}$ (Kieffer, 2007)). Moreover, the distance between the ice and the regolith will increase. Both radiation and convection can play a role in the transfer of heat through this gaseous layer. We can simulate this behavior as the conductive, radiative and convective transfer between two horizontal plates with the temperature of the plate below higher than the temperature of the plate above. The total flux of energy between the two plates is

$$\Sigma \text{Flux} = C_d + R_d + C_v \quad (31)$$

where C_d is the conductive flux, R_d the radiative flux and C_v the convective flux.

We can estimate

$$C_d = \lambda_{\text{gas}}^{\text{CO}_2} \frac{\partial T}{\partial z_{\text{gas}}} \quad (32)$$

z_{gas} takes into account the gas expansion. For the radiative exchange, we suppose here that ϵ is equal to 1 for the CO₂ ice and for the regolith at the interface in order to simplify the calculation:

$$R_d = \Delta(\sigma T^4) \quad (33)$$

where σ is the Stephan–Boltzmann constant and T the temperature at the regolith/CO₂ gas interface and at the CO₂ ice/CO₂ gas interface.

For the convective flux, we have first to determine the Rayleigh number (Ra), which is the product of the Grashof number (Gr) and the Prandtl number (Pr).

$$Ra = Gr Pr \quad (34)$$

$$Gr = \frac{g\beta\Delta T\Delta z_{\text{gas}}^3}{\nu^2} \quad (35)$$

$$Pr = \frac{C_p\mu}{\lambda} \quad (36)$$

where ν is the kinematic viscosity of CO₂, β the volumetric thermal expansion coefficient (equal to approximately $1/T$ for ideal fluids, where T is the temperature), g the gravity on Mars and Δz_{gas} the distance between the regolith/CO₂ gas interface and the CO₂ ice/CO₂ gas interface. $\nu = \frac{\mu}{\rho}$, where μ is the CO₂ gas viscosity ($1.1 \times 10^{-5} \text{ Pa s}$ at 160 K) and ρ the CO₂ gas density (0.125 kg m^{-3} at 162.8 K under a 0.6 m thick CO₂ ice slab for surface pressure equal to 507 Pa). We can estimate

$$Ra = 4.81 \times 10^6 \Delta T \Delta z_{\text{gas}}^3 \quad (37)$$

Since we are in the case of Rayleigh–Benard convection, the critical value of the Rayleigh number is estimated at 1707. We can assume a reasonable gas layer width of 2 cm (Kieffer, 2007). In this case, the critical value is obtained for $\Delta T = 44 \text{ K}$, which is one order of magnitude above the modeled gradient. We therefore assumed in our study that convection could be neglected.

To compute the effect of gas in the layer using the conduction equation (Eq. (22)), we kept the calculation as before, as if the ice and the regolith were in conductive contact, but used an equivalent conductivity between them which takes into account

- (1) the expansion of the gas and its conductivity,
- (2) the radiative flux.

We have

$$\lambda_{\text{eqgas}} \frac{\Delta T}{(1 - q_{\text{CO}_2})\Delta z} = \lambda_{\text{gas}} \frac{\Delta T}{(1 - q_{\text{CO}_2})\gamma\Delta z} + \sigma\Delta(T^4) \quad (38)$$

where γ is the expansion coefficient of CO₂ ($\gamma = \frac{\rho_{\text{solid}}}{\rho_{\text{gas}}}$) and q_{CO_2} the fraction of solid CO₂ in the layer. Rearranging,

$$\lambda_{\text{eqgas}} = \frac{\lambda_{\text{gas}}}{\gamma} + (1 - q_{\text{CO}_2})\Delta z\sigma \frac{\Delta(T^4)}{\Delta T} \quad (39)$$

When basal sublimation occurs, the last layer of CO₂ has both ice and gas. We have to calculate its new conductivity, which is given by

$$\lambda_{\text{eq}} = \frac{\Delta z}{\frac{q_{\text{CO}_2}\Delta z}{\lambda_{\text{solid}}} + \frac{(1 - q_{\text{CO}_2})\Delta z}{\lambda_{\text{eqgas}}}} \quad (40)$$

2.12. Gas ejection

In our model, we assume that in case of basal sublimation, when the gas amount reaches a threshold value (which can be chosen), the ice breaks, the gas is ejected in the atmosphere and the amount of gas at the base of the CO₂ slab is set to zero. This threshold value is set to 2 cm in the simulations, a reasonable value according to Kieffer (2007). However, it has no significant impact since it corresponds to a very small amount of gas which can form in only a few hours. Assuming no heat exchange during the ejection we have

$$\frac{T_{\text{exit}}}{T_{\text{soil}}(z)} = \left(\frac{P_{\text{surf}}}{P(z)}\right)^{\left(\frac{R_{\text{CO}_2}}{C_p}\right)} \quad (41)$$

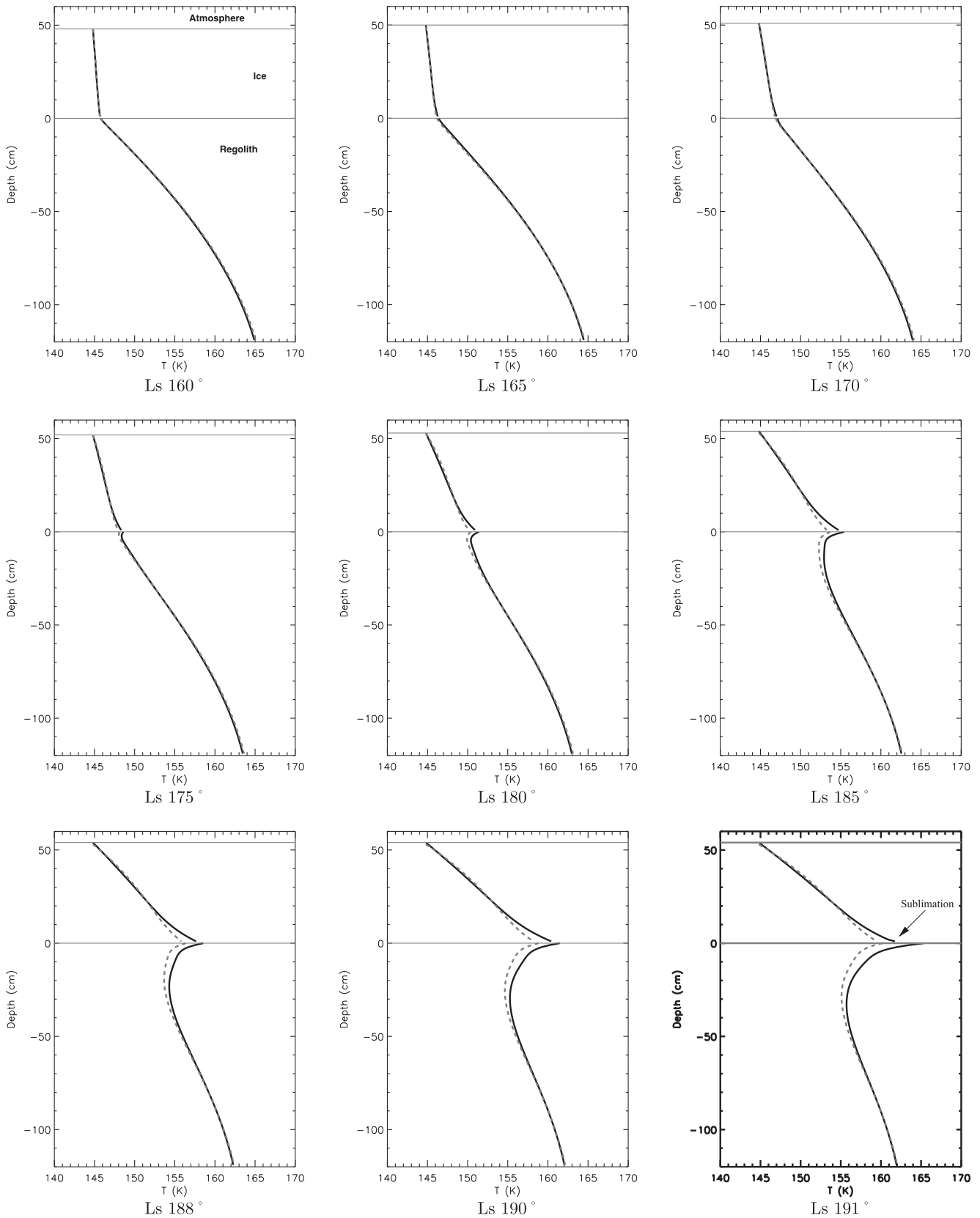


Fig. 8. Temperature profile at different Ls for clean CO₂ ice on a flat terrain (local time: 12 AM) at 85°S (late winter/early spring). Solid lines are simulations with a clean slab, dashed lines are simulations with a slab contaminated by 10 ppm of dust. Temperature at the regolith interface increases after the end of the polar night and basal sublimation begins at Ls 191°.

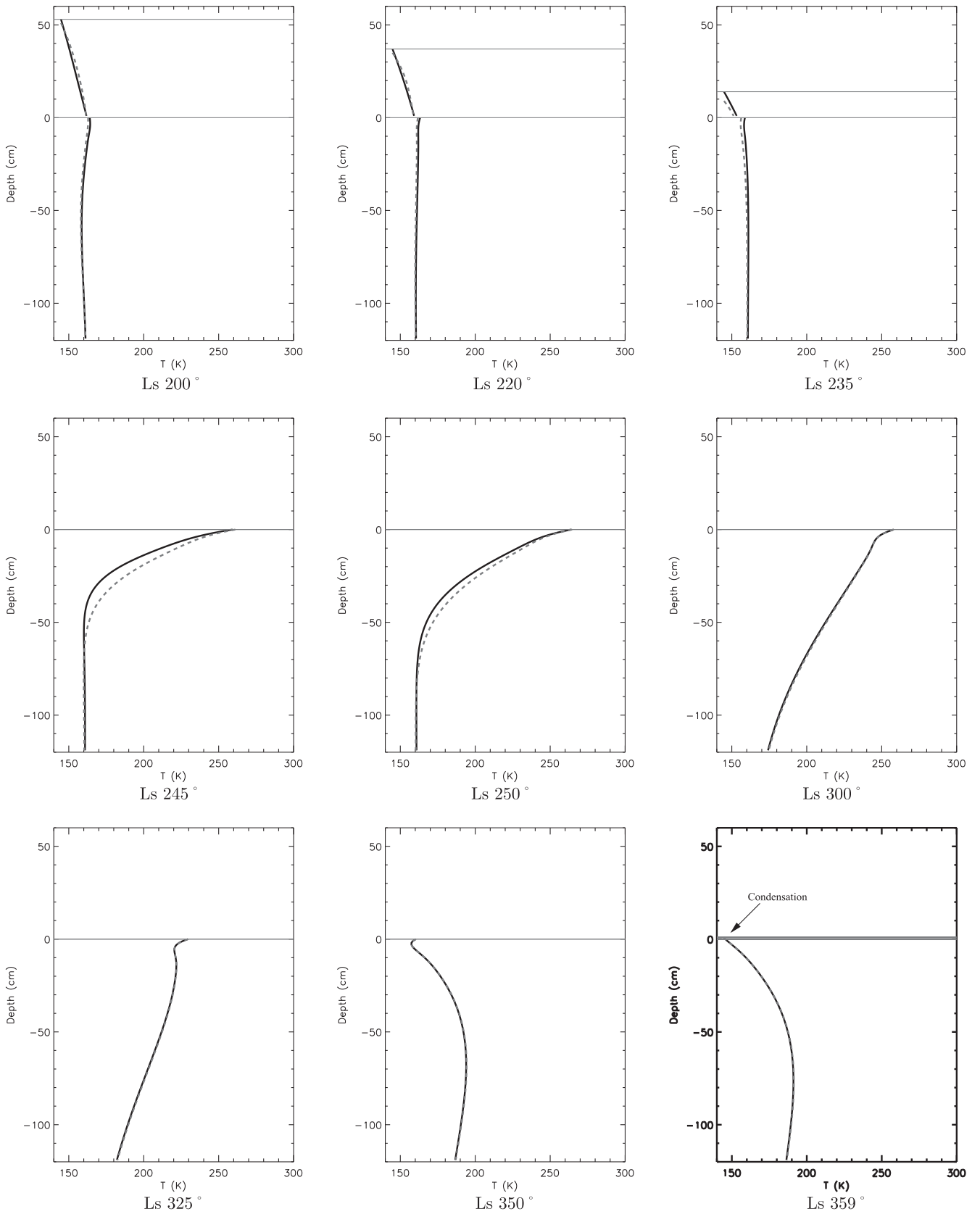


Fig. 9. Continuation of Fig. 8 (mid-spring to fall equinox). The x-axis limits have been changed to 145–300 K for clarity. CO₂ ice disappears at about Ls 240°. Then the surface quickly heats and reaches 260 K after a few martian days. During fall, surface temperature decreases down to the condensation temperature and CO₂ ice begins to accumulate.

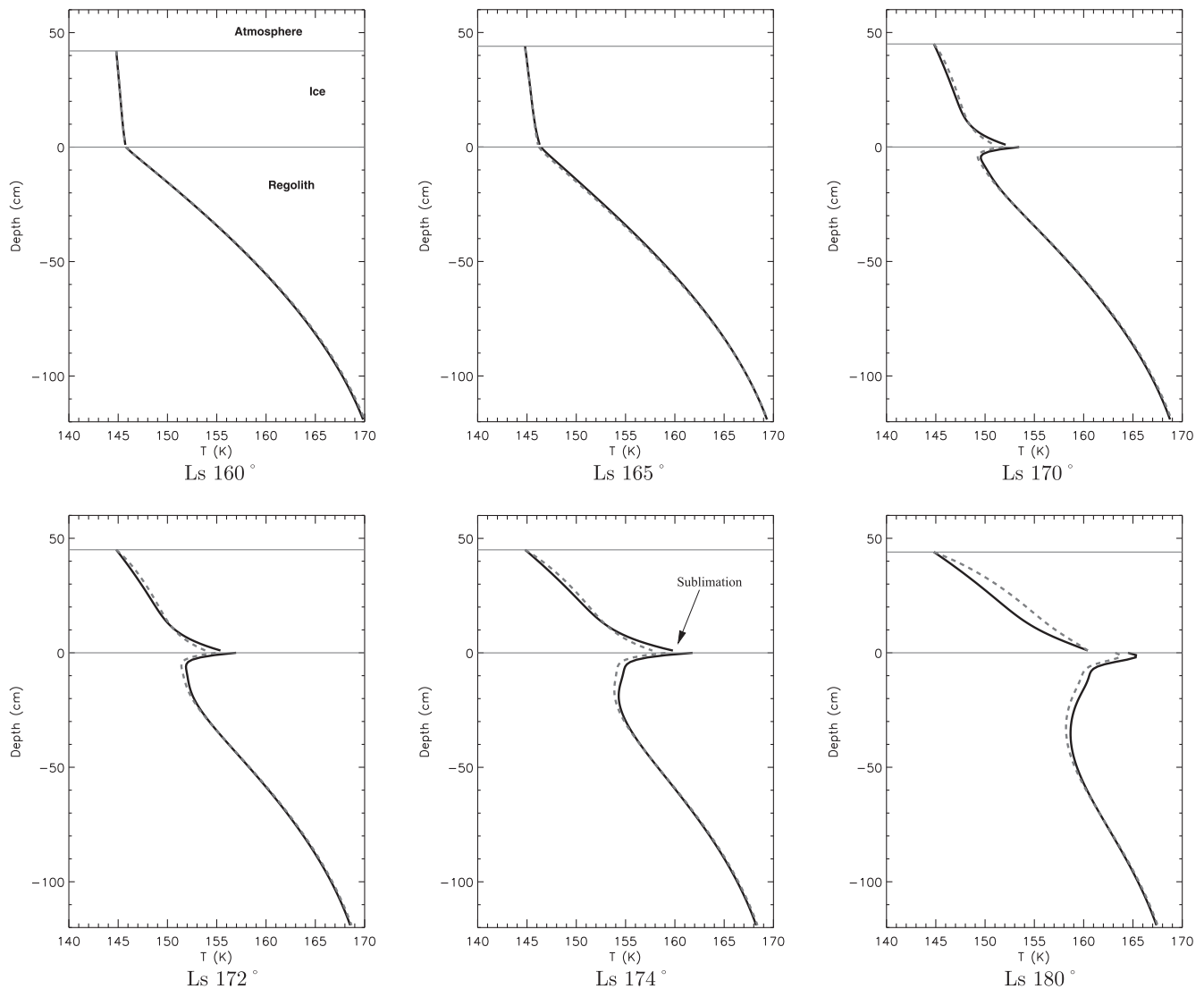


Fig. 10. Same as Fig. 8 but for a 30° north oriented slope (equator-facing). Temperature at the regolith interface increases much faster than for a flat terrain after the end of the polar night and basal sublimation begins at Ls 174°.

where T_{exit} is the temperature of the gas when it is ejected in the atmosphere, $T_{\text{soil}}(z)$ the temperature at the depth z where CO_2 ice is sublimated, P_{surf} the surface pressure, $P(z)$ the pressure of the gas at the depth z where CO_2 ice is sublimated, R_{CO_2} the specific gas constant of CO_2 , C_p the specific heat of CO_2 gas. Let us take a typical example with a 0.6 m thick CO_2 slab. Pressure at the base is close to 3985 Pa if the surface pressure is equal to 400 Pa (a typical surface pressure at 85°S latitude and Ls 180°). The temperature at the base of the slab is equal to the sublimation temperature in these conditions, i.e. 162.75 K. The calculation gives us an ejection temperature close to 98 K which means that, using this simple approach, we can estimate that about 7% of the ejected gas may recondense during the ejection:

$$\% \text{ of recondensation} = \frac{T_{\text{cond}} - T_{\text{exit}}}{L_{\text{cond}}^{\text{CO}_2}} C_p^{\text{gas}} \quad (42)$$

3. Results and application to the Manhattan Island region

3.1. The Manhattan Island region

The “Manhattan Island” region is centered at 99°E, 86.25°S, and follows the classic TES “cryptic” behavior of low albedo

while remaining near the CO_2 ice temperature (Kieffer et al., 2006). At this latitude, polar night begins at Ls 10° and ends at Ls 168°. The first dark spots appear very quickly after the end of the polar night. They can be seen in THEMIS images at Ls 176° (Kieffer et al., 2006). In this region, OMEGA spectra show that CO_2 ice consists of a thick slab, contaminated by dust in the upper layers (Langevin et al., 2007). This spectrum is typical of the cryptic region. OMEGA data were acquired between Ls 183° and Ls 192° and since dust may have been brought by the venting process, it is possible that a clean slab lay on the ground earlier, at the end of the polar night. According to our model, such a slab would be very translucent in the visible. For instance, with a solar incidence angle of 70°, about 3/4 of the flux reaches the base of the slab. We thus tried our model with this particular area. The main point here was to check if basal sublimation could occur and when.

3.2. Evolution of temperature

The following baseline parameters were chosen: slab model; uniform regolith thermal inertia: 200 SI; regolith albedo: 0.24; atmospheric dust optical depth: 0.1 (Vincendon et al., 2008,2009).

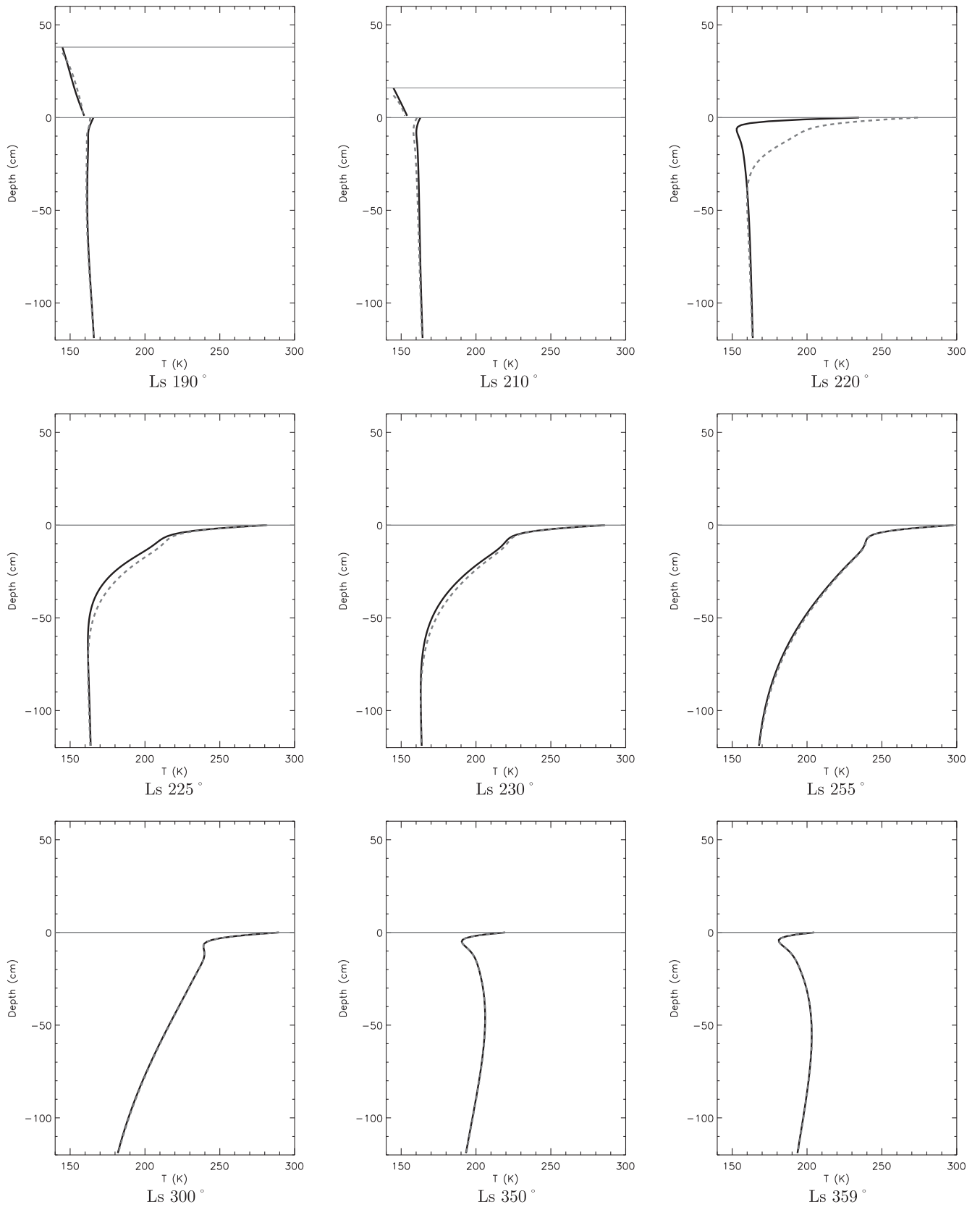


Fig. 11. Continuation of Fig. 10 (mid-spring to fall equinox). CO₂ ice disappears at about Ls 220°. Then the surface temperature quickly heats up and reaches 260 K after a few martian days and 290 K after about 50 martian days.

3.2.1. Simulation results on a flat terrain

Just after the end of the polar night, as the Sun is low on the horizon, the Fresnel reflection severely limits the direct solar flux penetration and temperatures remain near 145 K in the slab, as shown in Fig. 8. The total amount of CO₂ ice keeps growing even if sublimation at the surface has already begun during the day. As soon as the Sun is high enough in the sky, solar radiation penetrates down to the regolith interface where it is absorbed in the first few millimeters. Temperature increases quickly, and by thermal conduction, at the base of the CO₂ slab. Sublimation temperature at the base of the slab is reached at Ls 191°, during the afternoon. The ejection time occurs a few tens of minutes after the sublimation begins. Gas continues to form and to be vented out until the night comes and the temperature gets too low. The simulation results show that some energy is kept during the night in the slab. Therefore, each following day the energy that is needed for basal sublimation to occur decreases and the first gas ejection of the day is earlier than for the previous day. As shown by Fig. 8, adding dust, even a few ppm, has a significant impact on the results. Dust radically changes the slab's properties. For instance, a slab with a mass fraction of dust of 10 ppm absorbs about five times more solar radiation. That is the reason why temperature is higher in the slab when dust is present. However, a smaller fraction of solar radiation can reach the regolith and temperature increase at the interface is slower. "Crocus" day occurs at about Ls 245° in these simulations, which is quite early compared to the observations (more in the range of Ls 250–280°) (Kieffer et al., 2000; Langevin et al., 2007). We have to keep in mind that we simulate here a slab with constant properties, as we are mainly interested in simulating the onset of spot formation. In reality dust and CO₂ frost that are ejected change the optical properties of the slab. This optically thick layer of dust and frost stops the solar radiation and sublimation can occur only at the surface until wind removes this dust away and frost sublimates. Solar radiation can then penetrate in the slab again and basal sublimation can go on. After the "crocus" day, the surface temperature increases very quickly up to about 260 K as shown by Fig. 9. During fall, the surface temperature decreases down to the condensation point and CO₂ ice begins to form.

3.2.2. Simulation results on a 30° north oriented slope

For these simulations, we took into account a 30° north oriented slope (equator-facing). Processes involved in this simulation (Figs. 10 and 11) are quite similar to the previous one. However, since the angle between the direct incoming solar flux and the local vertical is slightly lower, Fresnel reflection is not that significant and a large part of the solar radiation can penetrate very early into the slab. As a result, first gas ejections can occur as early as Ls 174° which is consistent with the observations. We can notice (Fig. 10) that at Ls 174° (12 AM), gas ejection has not yet occurred (it will occur a few hours later). As for the flat terrain case, each day, the first gas ejection occurs earlier than for the previous day; at Ls 180°, the gas ejection already occurred. Since the gas layer acted like an insulator, energy was kept in the first regolith layers and was released after the gas ejection. This 30° north oriented slope case can actually be seen as a good way to represent a small-scale irregularity on a flat terrain.

4. Dark spots formation on Mars

We have shown in the previous section that basal sublimation could occur in the Manhattan Island area. We then investigated more general cases and tried to see how significant the different parameters are for initiating the venting process.

4.1. Mean effective grain size and the dust content

CO₂ ice properties are the key to the venting process. Fig. 12 shows that different scenarios will occur, depending on these properties (CO₂ ice grain size and dust content). In every case, sublimation occurs at the surface, but if solar radiation can penetrate deep in the ice, basal sublimation becomes possible.

4.1.1. Surface sublimation

Very clean small-grained ice has an albedo so high that there is not enough energy to entirely sublime the seasonal CO₂ ice layer and ice accumulates year after year (Fig. 12, zone 4). If we increase the grain size or add dust (Fig. 12, zone 3), we decrease the albedo and a CO₂ cycle consistent with the observed one is possible. Fig. 13 shows that the temperature remains near 145 K in the CO₂ slab until the "crocus" day. Solar radiation is absorbed in the first millimeters and sublimation only occurs at the surface.

4.1.2. Sublimation within the ice

If we continue to increase the effective grain size (more than a few millimeters) and limit the mass fraction of dust to less than a few hundreds of ppm (Fig. 12, zone 2), solar radiation begins to penetrate more deeply into the ice. Still, most of the energy is absorbed by the ice and very little can reach the regolith. Sublimation temperature can be reached within the ice, as shown in Figs. 14 and 15. CO₂ gas bubbles can form around and ice could eventually crack.

4.1.3. Basal sublimation

When the effective grain size is in the range of about 10 cm or more, and the mass fraction of dust is less than about 10–15 ppm (Fig. 12, zone 1), the fraction of solar radiation that reaches the regolith is sufficient for basal sublimation to occur. As we explained before, surface sublimation continues at the same time.

4.1.4. Diurnal cycle

Slab CO₂ ice and small-grained CO₂ ice have totally different behaviors with regard to the diurnal cycle, as can be seen in Figs. 16 and 17. With small-grained CO₂ ice, everything occurs at the surface, where the CO₂ ice layer is in equilibrium with the atmosphere and the CO₂ ice amount evolution is directly linked to the diurnal cycle. It decreases during the day and increases during

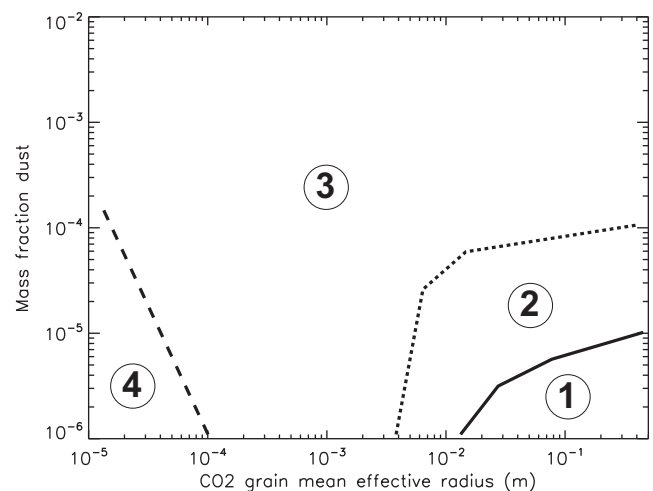


Fig. 12. Different behaviors of the CO₂ ice depending on effective grain size and dust content. Zone 1 represents the zone where both surface and basal sublimation occur; zone 2, is the same as zone 1 but here sublimation temperature is reached within the ice before being reached at the base; zone 3, the zone where only surface sublimation occurs; zone 4 the zone where CO₂ ice accumulates year after year. Simulations were run on a flat terrain at 85°S.

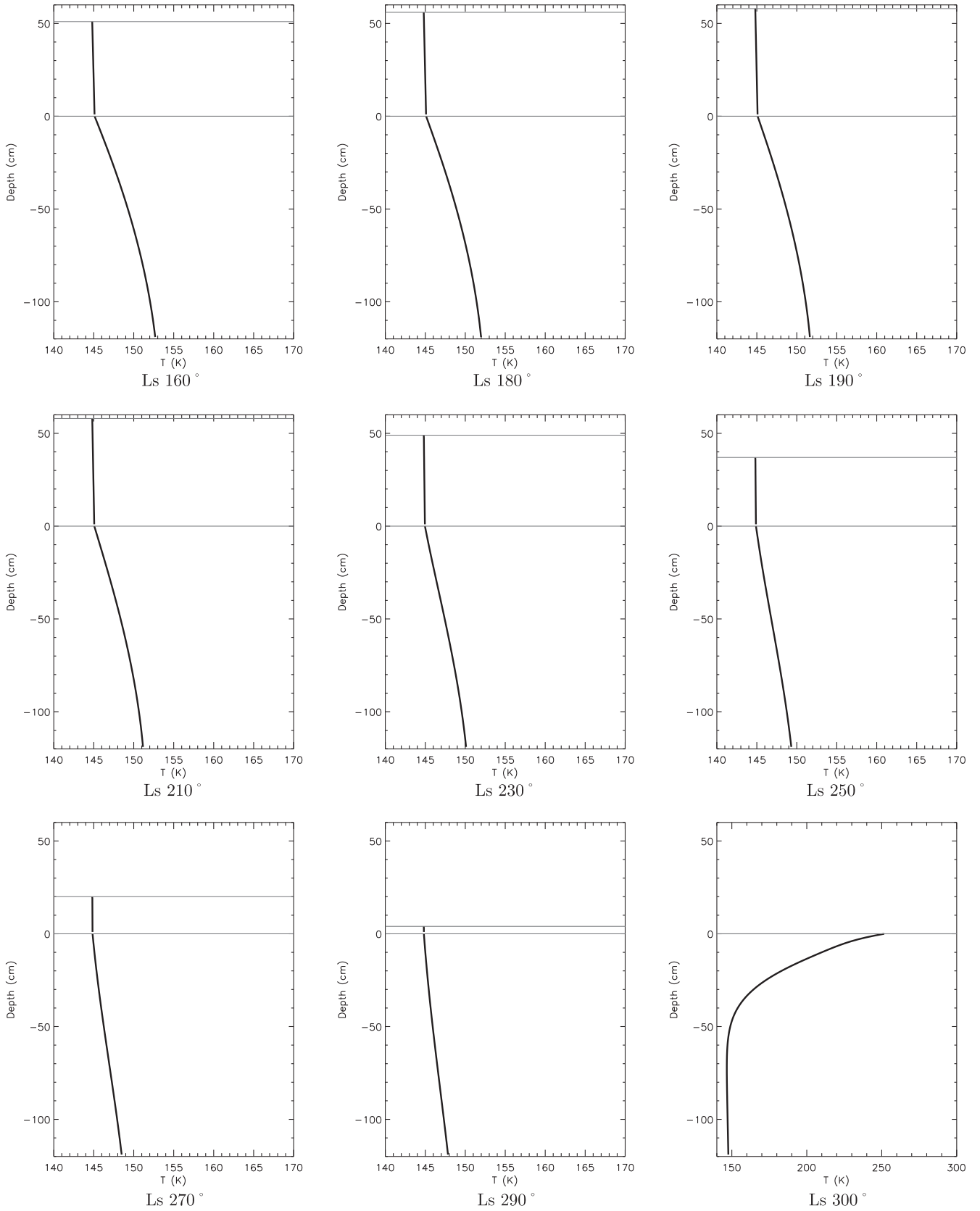


Fig. 13. Same as Fig. 8 but for small-grained CO₂ ice (effective radius: 130 μm, 200 ppm of dust). As the photons are not able to penetrate into the CO₂ ice, temperature within the ice stays close to 145 K. In this case, the albedo is higher than for slab ice and CO₂ ice does not disappear until about Ls 295°.

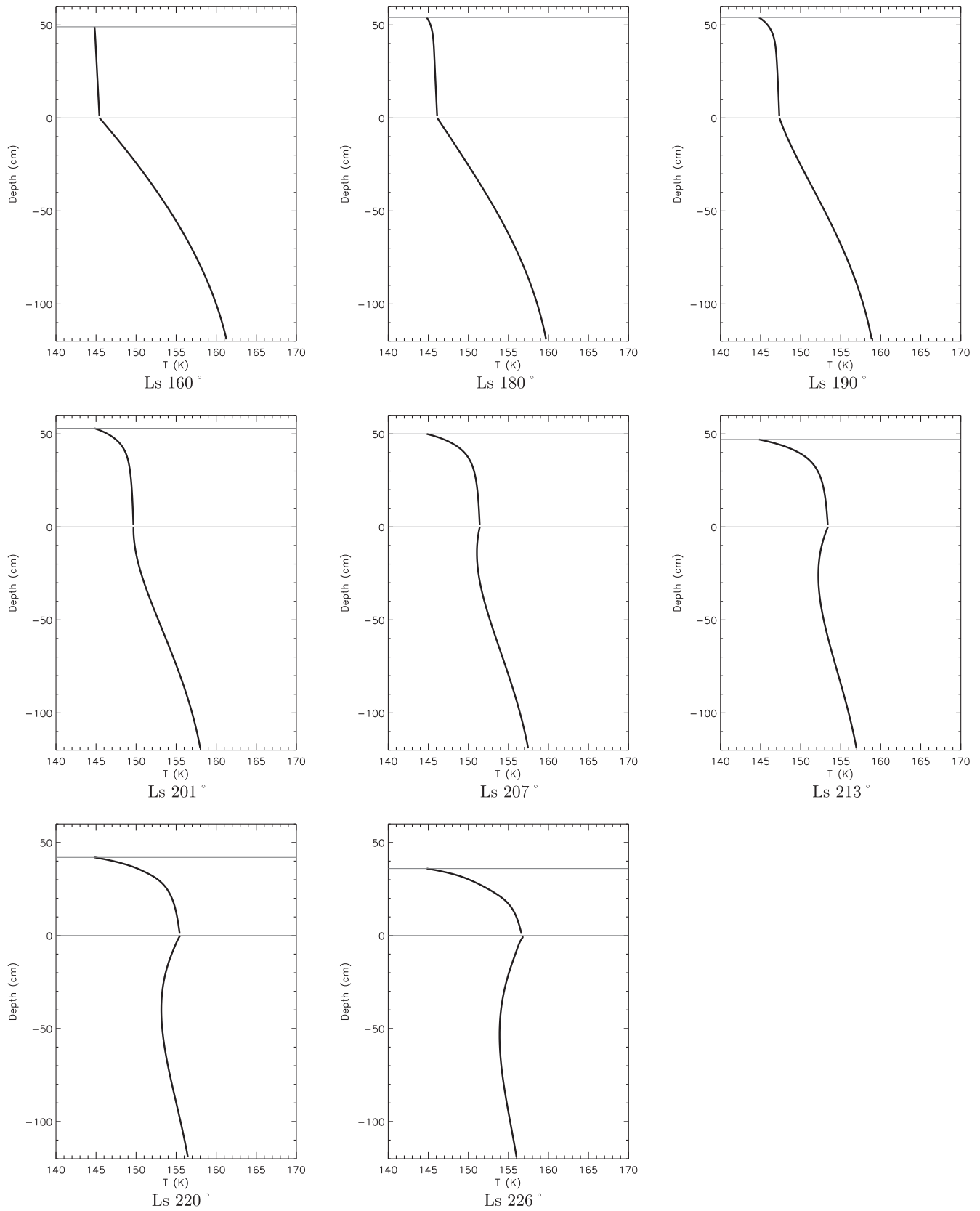


Fig. 14. Same as Fig. 8 but for CO_2 ice with an effective grain radius of 2.5 cm and a dust contamination of 10 ppm. Sublimation temperature is reached within the ice at about $L_s 218^\circ$. We limit the covered period here, since we think that gas bubbles will form around and ice will crack. CO_2 ice properties and involved processes will therefore change after that point.

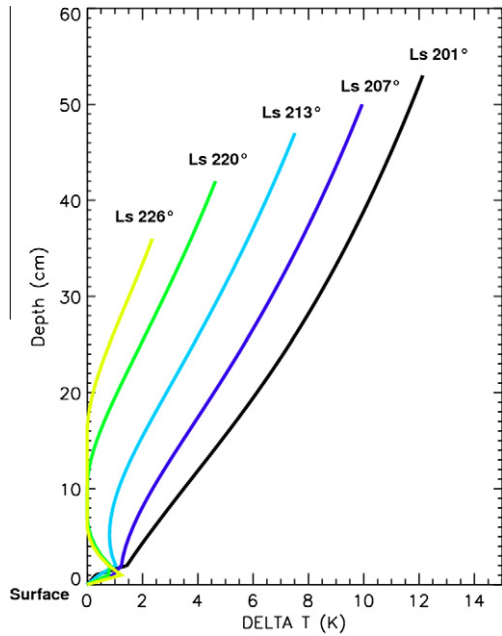


Fig. 15. Evolution of the difference between the sublimation temperature and the temperature within the CO₂ ice (same parameters as in Fig. 14). Sublimation temperature is reached at about 9 cm depth.

the night. However, in the case of the translucent slab scenario, the diurnal cycle has less influence on the sublimation and condensation processes. Only a small fraction of the solar flux is absorbed by the CO₂ ice. Most of the energy is absorbed by the regolith. Thus during the day, sublimation at the surface is limited. Thermal conduction, but also solar flux absorption in the CO₂ ice, leads to energy storage in the slab and condensation during the night is reduced (Fig. 17).

4.2. Effect of slope and orientation

Slope and orientation change the incidence angle of the photons, and therefore the Fresnel reflection which limits the solar flux

penetration. At high latitudes, the solar zenith angle is generally between 80° and 90° at the beginning of spring. Slope and orientation thus determine when a large fraction of the solar radiation begins to penetrate into the slab and thus when the first gas ejection will occur. In the case of Manhattan Island (85°S), Fig. 18 shows that the CO₂ ice maximum is about 15% smaller on a 30° north oriented slope than on a flat terrain, and the sublimation temperature at the base of the slab is therefore about 1 K lower. Furthermore, at Ls 175° for instance, solar zenith angle minimum is at about 86° (Fig. 2), which means that a maximum of 40% of the direct flux can penetrate into the slab for a flat terrain whereas more than 90% penetrates in the case of a 30° north oriented slope.

4.3. Regolith thermal inertia

Aharonson (2004) and Kieffer (2007) suggested that the seasonal thermal wave could be sufficient to cause CO₂ ice sublimation during the polar night. We did not observe any gas ejection in our simulations during the polar night, even when we considered a high thermal inertia (up to 2000 SI) that could be representative of an ice-rich near-surface. High thermal inertia certainly limits the CO₂ condensation but also makes the regolith heating much more difficult. Since the sublimation temperature at the interface is much greater than at the surface it is very difficult to reach it. Fig. 19 shows that increasing the thermal inertia of the regolith delays by up to 10° of Ls the starting date of CO₂ jet activity. Seasonal thermal waves can therefore not initiate the venting process on their own. Furthermore, according to our results, regolith thermal inertia does not have a large impact on the time of the first gas ejection (a few degrees of Ls) since both previously mentioned processes seem to compensate each other.

4.4. Regolith albedo

We ran tests with albedo values between 0.05 and 0.3 (realistic range for the martian soil). Fig. 20 shows a small increase (less than 5° of Ls for the albedo range) of the time needed to heat up the regolith as we increased the albedo.

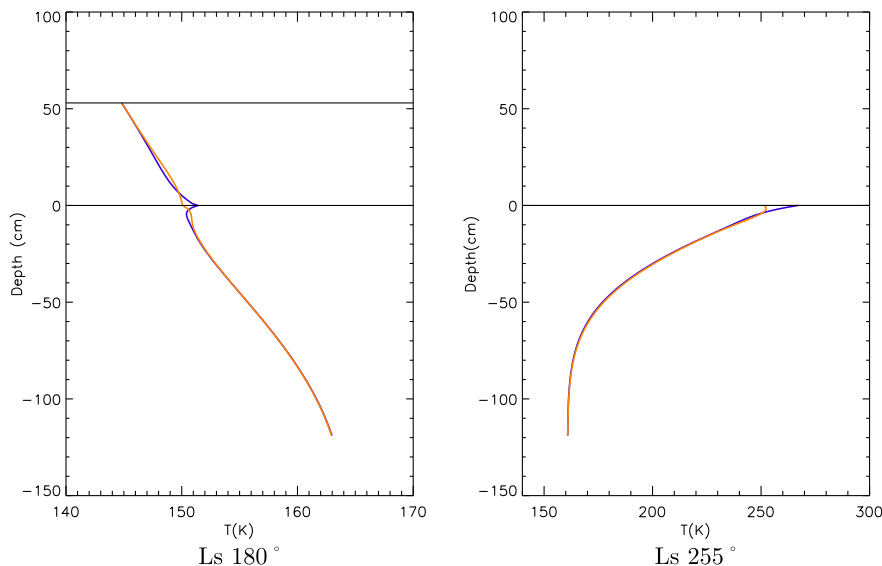


Fig. 16. Temperature profile at local 12 AM (blue) and 12 PM (orange) for a clean CO₂ ice slab on a flat terrain at 85°S. Energy storage in the slab is apparent. Furthermore, the largest temperature difference between 12 AM and 12 PM occurs at the regolith interface. Once CO₂ ice has disappeared, there are daily thermal waves. (For interpretation of the references to color in this figure legend, the reader is referred to the web version of this article.)

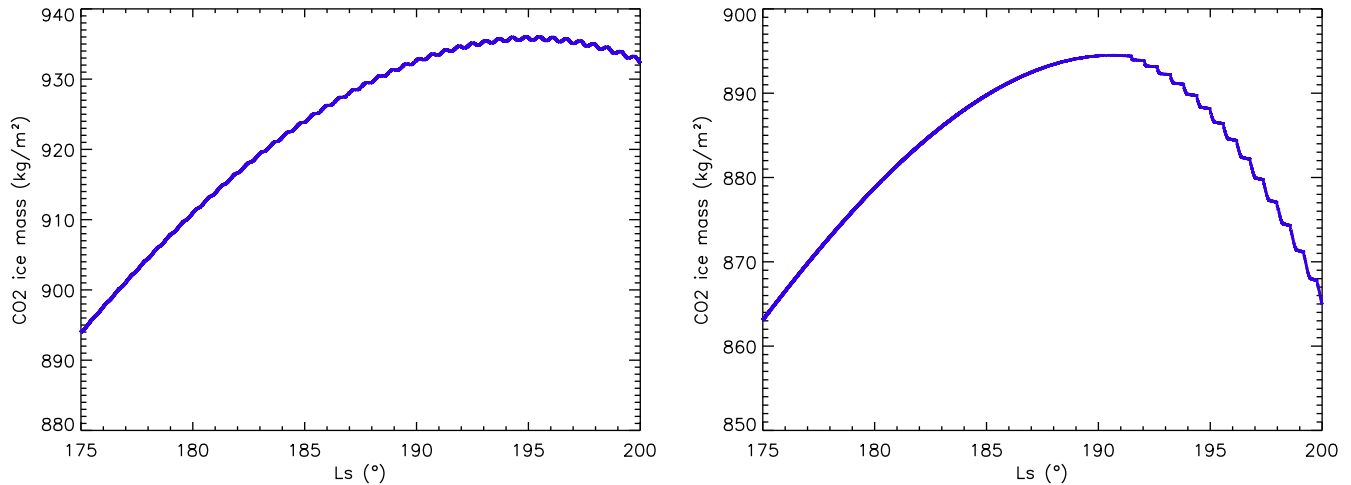


Fig. 17. Evolution of the amount of CO₂ ice for small-grained dusty (100 ppm) CO₂ ice (left) and a clean slab (right) at 85°S. Considering the plot on the left and the left part of this plot (before reaching the maximum), we can see that CO₂ ice condenses at night (the CO₂ ice amount increases) and CO₂ ice sublimates during the day (the CO₂ ice amount decreases). However, in the case of translucent CO₂ ice, the amount of CO₂ ice never decreases before reaching the maximum. This is due to the fact that the solar flux penetrates in the case of a translucent slab and does not appreciably slow the condensation process whereas this same flux sublimates the ice in the case of small grains with little penetration. After the end of the polar night, in the case of slab ice, energy storage makes condensation during the night very difficult to achieve.

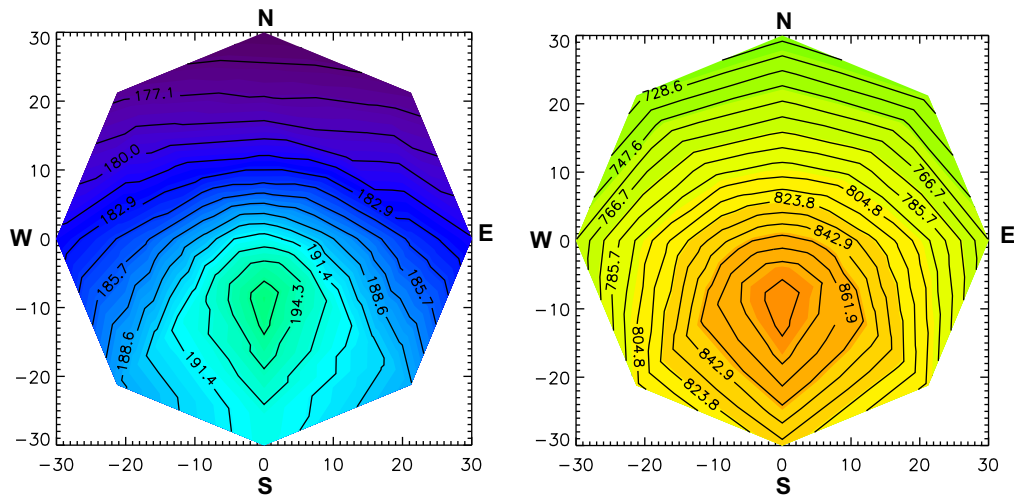


Fig. 18. Evolution of the solar longitude Ls (deg) of the first gas ejection with slope and orientation (left) and evolution of CO₂ ice maximum amount (kg m⁻²) (right) at 85°S (slab model is used). Both are directly linked to the insolation and therefore present similar patterns. We can notice that basal sublimation can occur on pole-facing slopes.

4.5. Latitude

Simulations were also run at different latitudes (Fig. 21). Atmospheric dust optical depth was kept to 0.1. Surface pressure was set to 400 Pa in the southern hemisphere and to 1000 Pa in the northern hemisphere. This higher pressure in the north tends to increase the maximum amount of CO₂ ice. This explains why CO₂ ice maxima are rather close in north and south polar regions in spite of the fact that the southern polar night is longer. The time of initiation of the venting process evolves with latitude, as a function of the incident solar radiation.

5. Discussion

5.1. Manhattan Island region scenario

CO₂ ice may have some dust inclusions when the first solar beams penetrate, about 10° of Ls before the end of the polar night. The solar radiation remains too low to significantly heat the regolith at that time, but its heating may clean the slab, as described in Kieffer (2007) and Portyankina et al. (2010). Thus, at the end of the polar night, when the solar radiation is

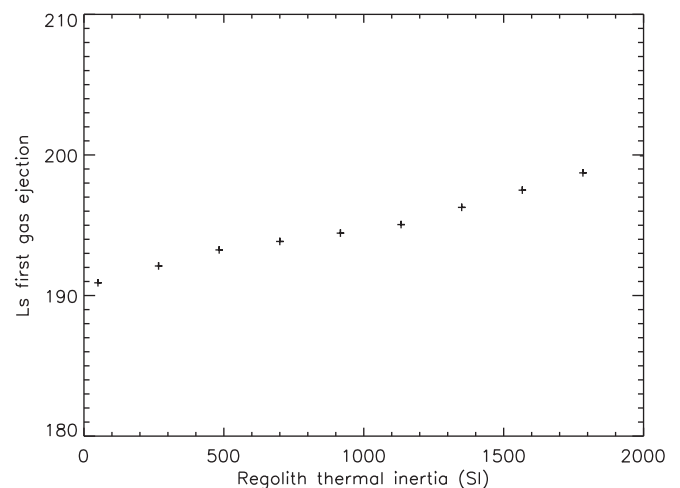


Fig. 19. Evolution of the solar longitude Ls (deg) of the first gas ejection with respect to the regolith thermal inertia at 85°S (slab model). Contrary to what was expected, increasing the regolith thermal inertia does not accelerate the beginning of the venting process but delays it (less than 10° of Ls in the considered range).

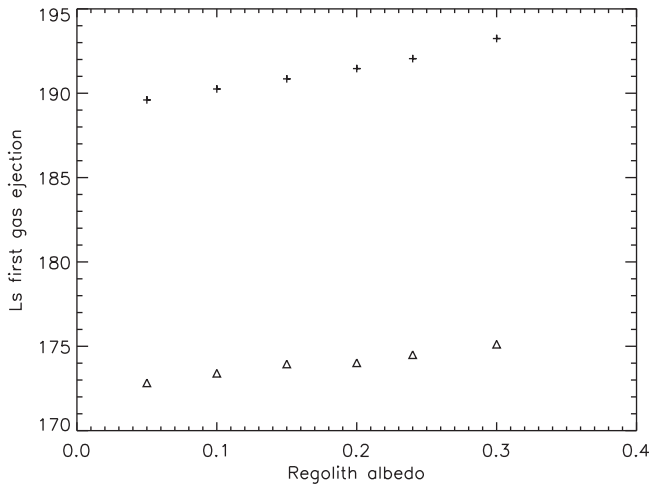


Fig. 20. Evolution of the solar longitude Ls (deg) of the first gas ejection with respect to the regolith albedo at 85°S for a flat terrain (crosses) and for a 30° north oriented slope (triangles). Slab model is used. Since the slab is translucent, a large part of the energy reaches the regolith. Therefore, when we decrease the albedo, the fraction of the solar flux that penetrates into the regolith does not increase enough to accelerate significantly the beginning of the venting process.

significantly higher, the slab is probably translucent and the clean slab scenario is appropriate. A large fraction of solar radiation can penetrate as soon as polar night ends on small-scale irregularities (equator facing slopes) and initiates the venting process. The regolith quickly heats up and sublimation temperature is reached at the base of the CO₂ slab as early as Ls 174°. During the day, gas continues to form and to be ejected. At night, sublimation stops until the following day when sublimation temperature can be reached again. When frost and dust cover the ice, solar radiation cannot penetrate as easily anymore. However, basal sublimation can continue outside the dark spot. As the slab has already been weakened by the first gas ejection, it is likely that sublimated CO₂ will try to escape by the same path. As the CO₂ ice amount decreases, pressure difference between the surface and the base of the slab decreases. Gas and dust ejection is therefore less and less violent and less dust or substrate material is expelled outside. Near Ls 260°, “crocus” day occurs: CO₂ disappears and regolith heats up to 260 K in a few days.

5.2. Venting process on Mars

Several areas with slab ice have been observed at different latitudes on Mars. Our simulations tend to show that for similar conditions, basal sublimation can occur at every latitude. Of course,

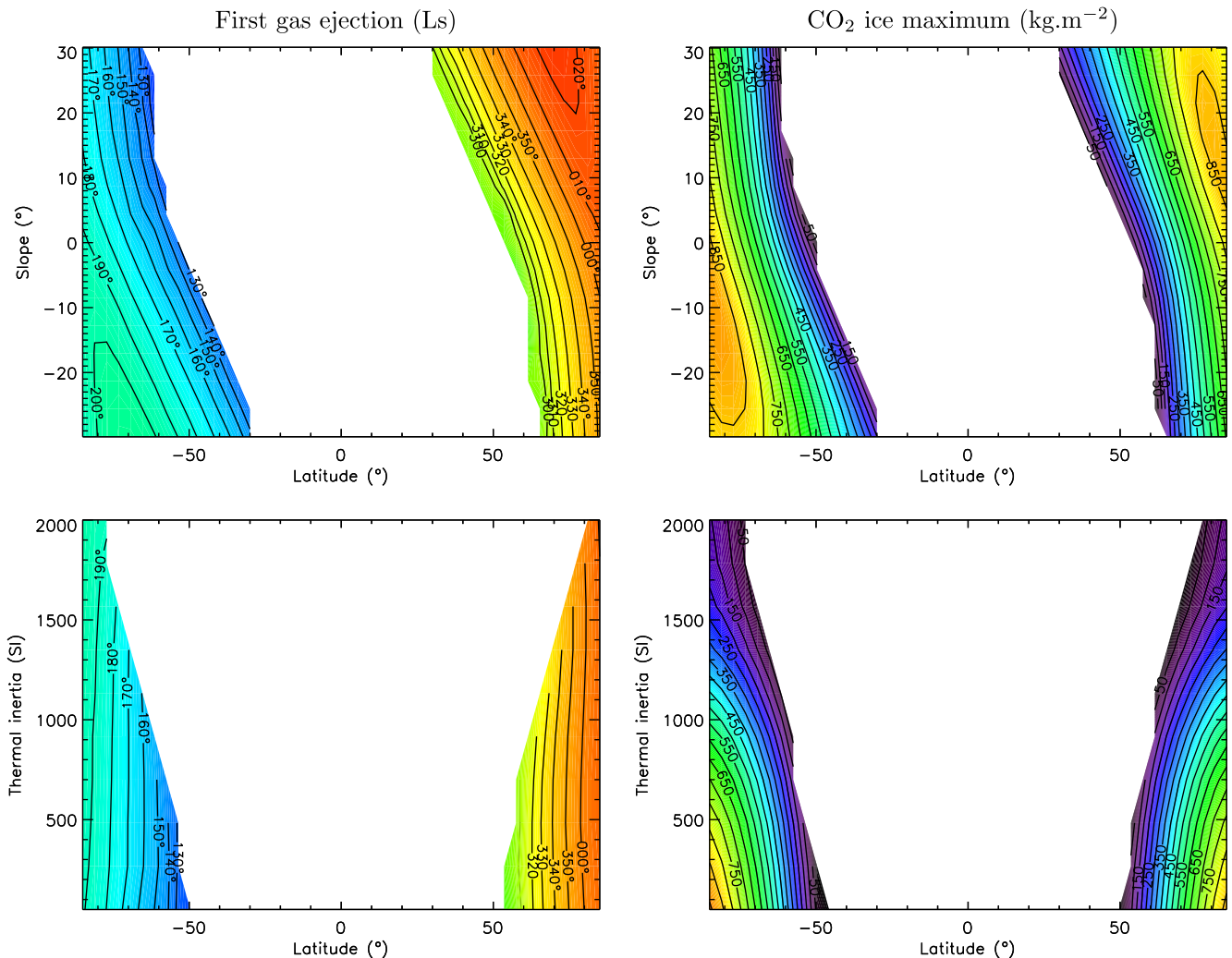


Fig. 21. Evolution of the solar longitude Ls (deg) of the first gas ejection and of CO₂ ice maximum amount with respect to the latitude (slab model). Surface pressure was set to 400 Pa in the southern hemisphere and to 1000 Pa in the northern hemisphere. Results show that the venting process can also occur in the northern hemisphere.

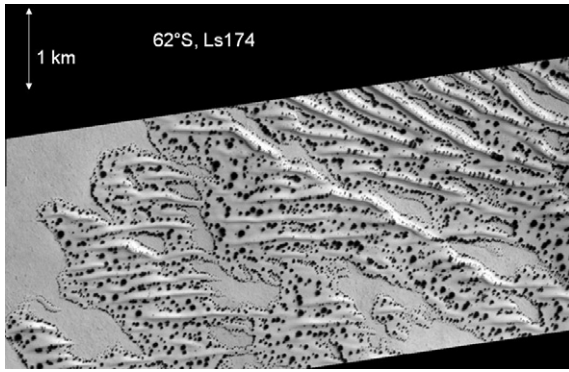


Fig. 22. MOC image of a dune field at 62°S and Ls 174°. Dark spots seem to be present only on dunes.

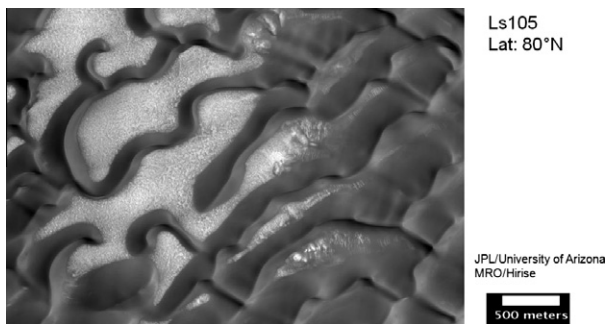


Fig. 23. HiRISE image of a dune field at 80°N and Ls 105°. We can notice the albedo difference between dune material and the surroundings, since the seasonal CO₂ ice cap has disappeared.

the effect will not be the same at 85°S where there may be a 60 cm thick slab and at 50°S where it will not be thicker than 10 cm. Indeed the difference of pressure between the bottom of the slab and the surface will be totally different. At mid-latitudes, where there is much less ice, gas ejection will be less energetic and there will be less (or no) ejected dust and substrate material. The main result is that as long as we have similar conditions (ice properties, albedo, regolith thermal inertia, etc.), gas ejections are as likely to occur in the north as in the south. Kieffer and Titus (2001) and Piqueux and Christensen (2008) report evidence of active venting processes in the north which confirm our results. However, water ice is much more abundant in north polar regions and certainly plays a role. Adding water ice inclusions in our model should allow us to investigate more deeply dark spot formation in these regions.

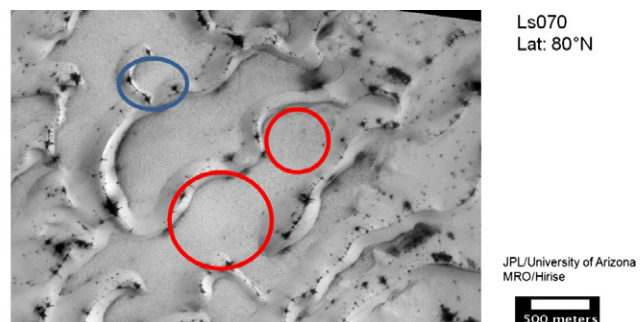
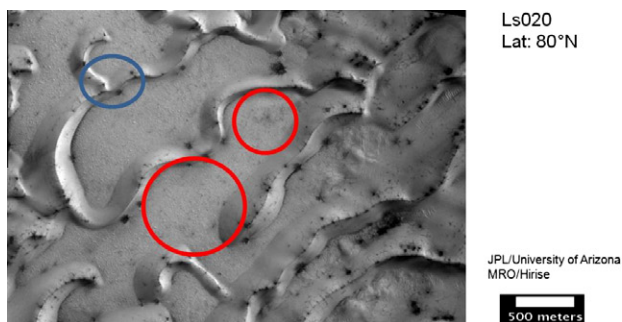


Fig. 24. HiRISE image of the same dune field as in Fig. 23, but at different Ls. Dark spots are clearly visible on dunes (blue circle). Some gray patterns are also visible around at Ls 20° and possibly at Ls 70° (red circles) in the surrounding terrain. (For interpretation of the references to color in this figure legend, the reader is referred to the web version of this article.)

5.3. Dark spots on dunes

One interesting question with dark spots is that when we look at an area with dune fields, they often seem to appear only on dunes (see Fig. 2 in Kieffer (2007) and Fig. 22 in this article). Can we explain this behavior with our model? Dunes have generally a lower albedo than the surrounding terrains (less than 0.2), a lower thermal inertia due to smaller grained material (as low as 50 SI) and present some slopes (Fig. 23). Model results show that gas ejections on the surrounding terrains should occur about 10–20° of Ls after the ones on the dunes. The model cannot explain why dark spots seem to occur only on dunes. Whether gas ejection occurs or not is determined by CO₂ ice properties, which are expected to be similar both on dunes and the surroundings (see previous sections). We think that gas ejections also occur around dunes but are much more difficult to detect due to differences in the substrate material. Dunes are composed of dark sand and the dust grains that cover the surrounding terrains have a higher albedo, as can be seen in Fig. 23. In the case of a gas ejection, some substrate material is brought up by the gas and ejected. The substrate material forms a dark spot surrounded by bright CO₂ frost. We thus suggest that gas ejections first occur on dunes and that dark and large spots appear. A little bit later, gas ejection begins to occur on surrounding terrains and dust is ejected. Considering the difference of albedo, it is more difficult to detect dust than dark sand on the CO₂ ice deposit. Still, in both cases bright patches due to CO₂ recondensation should form. The results that we present here are consistent with previous HiRISE observations of dunes fields (Fig. 24).

5.4. Cracks within the ice

As explained previously, we found that the sublimation temperature could be reached within the CO₂ ice under certain conditions. We suggest the following interpretation for such a phenomenon: CO₂ gas bubbles form at the interfaces, which means around the dust, H₂O and CO₂ small grains. Pressure around these interfaces increases and causes cracks in the ice. These cracks anneal during the cooler portion of the diurnal cycle, especially as the slab becomes cleaner following the likely ejection of the dust particles that induced them. This means that CO₂ ice properties do not remain constant: the CO₂ ice effective grain radius decreases as cracks appear within the ice. Fig. 12 should therefore be seen as a dynamic diagram. CO₂ ice composition and properties evolve with time. For instance, if sublimation within the ice was possible at a given time, cracks would cause a decrease of the effective radius, leading to totally different ice properties. This mechanism could be a clue to understand the decrease of the mean effective grain radius observed during spring in some areas of the southern

polar cap (Langevin et al., 2007). Different ice properties would lead to different sublimation processes, that could themselves change these ice properties. This interpretation is highly speculative and needs further study to be repudiated or confirmed, but raises an interesting concern about the CO₂ ice dynamics on Mars.

6. Conclusion

- (1) Only in the case of very large CO₂ grains and very little dust contamination, can a large fraction of solar radiation reach the regolith. In this latter case, the model shows that the regolith surface can heat and sublimation temperature at the base of the CO₂ ice can be reached, which is consistent with Kieffer (2007).
- (2) Simulation results show that the occurrence of basal sublimation during spring only depends on the CO₂ ice properties, considering that the substrate on which the CO₂ ice lies has an albedo lower than 0.3. Other parameters (thermal inertia, slope angle), however, have a significant impact on the starting date of the jet activity.
- (3) Early dark spot formation in Manhattan Island region (85°S) cannot be explained by seasonal thermal waves. However, our results show that the venting process can under certain conditions be initiated very early by solar radiation penetration and that dark spots could form as early as Ls 174°.
- (4) We suggest that the venting process also occurs around the dunes. However, substrate material nature make them certainly difficult to observe compared to the dark spots on the dunes.
- (5) We suggest that the decrease of the CO₂ ice effective grain radius observed during spring in some of the southern polar regions could be caused by cracks in the ice, which would be the result of sublimation within the ice.

In our simulations, we considered CO₂ ice with homogeneous and constant properties (grain size, dust inclusions) through time. Adding the possibility to have non-homogeneous and evolving ice should allow us to investigate in the future the differences between the cryptic and in the anticryptic regions. Furthermore, better knowledge about the nature and properties of the CO₂ ice during winter and its evolution with time would also be required to improve the simulations.

Acknowledgments

We would like to thank B. Schmitt for making his optical CO₂ ice properties available. We are also grateful to P.Y. Meslin, Y. Langevin, S. Douté, A. Spiga, and all our colleagues at LMD for inspiration and advice. Finally, we would like to thank H. Kietter and an anonymous Reviewer for useful comments and suggestions.

References

- Aharonson, O., 2004. Sublimation at the base of a seasonal CO₂ slab on Mars. In: Mackwell, S., Stansbery, E. (Eds.), *Lunar and Planetary Institute Science Conference Abstracts*, vol. 35, Abstract 1918.
- Bibring, J. et al., 2004. Perennial water ice identified in the south polar cap of Mars. *Nature* 428, 627–630.
- Forget, F., Hourdin, F., Talagrand, O., 1998. CO₂ snow fall on Mars: Simulation with a general circulation model. *Icarus* 131, 302–316.
- Forget, F., Hourdin, F., Fournier, R., Hourdin, C., Talagrand, O., Collins, M., Lewis, S.R., Read, P.L., Huot, J.-P., 1999. Improved general circulation models of the martian atmosphere from the surface to above 80 km. *J. Geophys. Res.* 104, 24155–24176.
- Hansen, G.B., 1999. Control of the radiative behavior of the martian polar caps by surface CO₂ ice: Evidence from Mars Global Surveyor measurements. *J. Geophys. Res.* 104, 16471–16486.
- Hansen, G.B., 2005. Ultraviolet to near-infrared absorption spectrum of carbon dioxide ice from 0.174 to 1.8 μm. *J. Geophys. Res. (Planets)* 110, E11003.
- Hourdin, F., Le Van, P., Forget, F., Talagrand, O., 1993. Meteorological variability and the annual surface pressure cycle on Mars. *J. Atmos. Sci.* 50, 3625–3640.
- James, P.B., Kieffer, H.H., Paige, D.A., 1992. The seasonal cycle of carbon dioxide on Mars. In: *Mars*. University of Arizona Press, Tucson, pp. 934–960.
- Kieffer, H.H., 2007. Cold jets in the martian polar caps. *J. Geophys. Res.* 112, E08005.
- Kieffer, H.H., Titus, T.N., 2001. TES mapping of Mars' north seasonal cap. *Icarus* 154, 162–180.
- Kieffer, H.H., Titus, T.N., Mullins, K.F., Christensen, P.R., 2000. Mars south polar spring and summer behavior observed by TES: Seasonal cap evolution controlled by frost grain size. *J. Geophys. Res.* 105, 9653–9700.
- Kieffer, H.H., Christensen, P.R., Titus, T.N., 2006. CO₂ jets formed by sublimation beneath translucent slab ice in Mars' seasonal south polar ice cap. *Nature* 442, 793–796.
- Langevin, Y., Douté, S., Vincendon, M., Poulet, F., Bibring, J.-P., Gondet, B., Schmitt, B., Forget, F., 2006. No signature of clear CO₂ ice from the 'cryptic' regions in Mars' south seasonal polar cap. *Nature* 442, 790–792.
- Langevin, Y., Bibring, J.-P., Montmessin, F., Forget, F., Vincendon, M., Douté, S., Poulet, F., Gondet, B., 2007. Observations of the south seasonal cap of Mars during recession in 2004–2006 by the OMEGA visible/near-infrared imaging spectrometer on board Mars Express. *J. Geophys. Res.* 112, E08S12.
- Malin, M.C., Edgett, K.S., 2000. Frosting and defrosting of martian polar dunes. In: *Lunar and Planetary Institute Science Conference Abstracts*, vol. 31. Lunar and Planetary Inst. Technical Report, Abstract 1056.
- Ockert-Bell, M.E., Bell III, J.F., McKay, C., Pollack, J., Forget, F., 1997. Absorption and scattering properties of the martian dust in the solar wavelengths. *J. Geophys. Res.* 102, 9039–9050.
- Piqueux, S., Christensen, P.R., 2008. North and south subice gas flow and venting of the seasonal caps of Mars: A major geomorphological agent. *J. Geophys. Res. (Planets)* 113, E06005.
- Piqueux, S., Byrne, S., Richardson, M.I., 2003. Sublimation of Mars's southern seasonal CO₂ ice cap and the formation of spiders. *J. Geophys. Res.* 108 (E8), 5084.
- Portyankina, G., Markiewicz, W.J., Thomas, N., Hansen, C.J., Milazzo, M., 2010. HiRISE observations of gas sublimation-driven activity in Mars southern polar regions: III. Models of processes involving translucent ice. *Icarus* 205, 311–320.
- Quirico, E., Schmitt, B., 1997. A spectroscopic study of CO diluted in N₂ ice: Applications for Triton and Pluto. *Icarus* 128, 181–188.
- Schmitt, B., Quirico, E., Trotta, F., Grundy, W.M., 1998. Optical Properties of Ices from UV to Infrared. In: B. Schmitt, C. de Bergh, & M. Festou (Ed.), *Solar System Ices*. Vol. 227 of *Astrophysics and Space Science Library*. 199.
- Schubert, G., Solomon, S.C., Turcotte, D.L., Drake, M.J., Sleep, N.H., 1992. Origin and thermal evolution of Mars. *Mars*, 147–183.
- Spiga, A., Forget, F., 2008. Fast and accurate estimation of solar irradiance on martian slopes. *Geophys. Res. Lett.*, 35, L15201.
- Supulver, K.D., Edgett, K.S., Malin, M.C., 2001. Seasonal changes in frost cover in the martian south polar region: Mars Global Surveyor MOC and TES monitoring of the Richardson Crater dune field. In: *Lunar and Planetary Institute Science Conference Abstracts*, vol. 32 of *Lunar and Planetary Inst. Technical Report*, Abstract 1966.
- Toon, O.B., McKay, C.P., Ackerman, T.P., Santhanam, K., 1989. Rapid calculation of radiative heating rates and photodissociation rates in inhomogeneous multiple scattering atmospheres. *J. Geophys. Res.* 94, 16287–16301.
- Vincendon, M., Langevin, Y., 2010. A spherical Monte-Carlo model of aerosols: Validation and first applications to Mars and Titan. *Icarus* 207, 923–931.
- Vincendon, M., Langevin, Y., Poulet, F., Bibring, J.-P., Gondet, B., 2007. Recovery of surface reflectance spectra and evaluation of the optical depth of aerosols in the near-IR using a Monte Carlo approach: Application to the OMEGA observations of high-latitude regions of Mars. *J. Geophys. Res.* 112, E08S13.
- Vincendon, M., Langevin, Y., Poulet, F., Bibring, J.-P., Gondet, B., Jouglet, D., OMEGA Team, 2008. Dust aerosols above the south polar cap of Mars as seen by OMEGA. *Icarus* 196, 488–505.
- Vincendon, M., Langevin, Y., Douté, S., Bibring, J., 2009. 3 Mars years of dust optical depth mapping by OMEGA above the south pole. *LPI Contrib.* 1494, 59–60.
- Warren, S.G., 1986. Optical constants of carbon dioxide ice. *Appl. Opt.* 25, 2650–2674.
- Warren, S.G., Wiscombe, W.J., Firestone, J.F., 1990. Spectral albedo and emissivity of CO₂ in martian polar caps: Model results. *J. Geophys. Res.* 95, 717–741.
- Williams, K.E., Toon, O.B., Heldmann, J.L., McKay, C., Mellon, M.T., 2008. Stability of mid-latitude snowpacks on Mars. *Icarus* 196, 565–577.
- Wolff, M.J., Smith, M.D., Clancy, R.T., Arvidson, R., Kahre, M., Seelos, F., Murchie, S., Savijärvi, H., 2009. Wavelength dependence of dust aerosol single scattering albedo as observed by the Compact Reconnaissance Imaging Spectrometer. *J. Geophys. Res. (Planets)* 114, E00D04.